Bulletin of the Seismological Society of America, Vol. 98, No. 2, pp. 861–889, April 2008, doi: 10.1785/0120060411

Ⓔ

Late Holocene Rupture of the Northern San Andreas Fault and Possible Stress Linkage to the Cascadia Subduction Zone

by Chris Goldfinger, Kelly Grijalva, Roland Bürgmann, Ann E. Morey, Joel E. Johnson, C. Hans Nelson, Julia Gutiérrez-Pastor, Andrew Ericsson,[*] Eugene Karabanov,[†] Jason D. Chaytor,[‡] Jason Patton, and Eulàlia Gràcia

Abstract We relate the late Holocene northern San Andreas fault (NSAF) paleoseismic history developed using marine sediment cores along the northern California continental margin to a similar dataset of cores collected along the Cascadia margin, including channels from Barclay Canyon off Vancouver Island to just north of Monterey Bay. Stratigraphic correlation and evidence of synchronous triggering imply earthquake origin, and both temporal records are compatible with onshore paleoseismic data. In order to make comparisons between the temporal earthquake records from the NSAF and Cascadia, we refine correlations of southern Cascadia great earthquakes, including the land paleoseismic record.

Along the NSAF during the last ~2800 yr, 15 turbidites, including one likely from the great 1906 earthquake, establish an average repeat time of ~200 yr, similar to the onshore value of ~240 yr. The combined land and marine paleoseismic record from the southern Cascadia subduction zone includes a similar number of events during the same period. While the average recurrence interval for full-margin Cascadia events is ~520 yr, the southern Cascadia margin has a repeat time of ~220 yr, similar to that of the NSAF. Thirteen of the 15 NSAF events were preceded by Cascadia events by ~0–80 yr, averaging 25–45 yr (as compared to ~80–400 yr by which Cascadia events follow the NSAF).

Based on the temporal association, we model the coseismic and cumulative postseismic deformation from great Cascadia megathrust events and compute related stress changes along the NSAF in order to test the possibility that Cascadia earthquakes triggered the penultimate, and perhaps other, NSAF events. The Coulomb failure stress (CFS) resulting from viscous deformation related to a Cascadia earthquake over ~60 yr does not contribute significantly to the total CFS on the NSAF. However, the coseismic deformation increases CFS on the northern San Andreas fault (NSAF) by up to about 9 bars offshore of Point Delgada, most likely enough to trigger that fault to fail in north-to-south propagating ruptures.

Online Material: Relative timing of NSAF and Cascadia events and estimated Cascadia slip models.

Introduction

The development of long paleoseismic records along major fault systems allows correlation of records along strike and can establish spatial histories of rupture length. Combined with age data, long-correlated records can also address clustering, the applicability of slip-predicable or time-predicable models, and the nature of long-term stress interactions (e.g., Stein *et al.*, 1992; Ward and Goes, 1993; Weldon *et al.*, 2004). We have been using the marine turbidite record as a proxy for earthquake recurrence in both the Cascadia Subduction Zone, and on the northern San Andreas fault (NSAF) (Goldfinger *et al.*, 2003a, 2007). In comparison

[*]Present address: Continental Energy Corporation, Indonesia, Jl. Kenanga #62, Cilandak Jakarta, 12560, Indonesia.

[†]Present address: Chevron Energy Technology Company, Earth Science Technology Department, 1500 Louisiana St., Houston, Texas 77002.

[‡]Present address: Department of Geology and Geophysics, Woods Hole Oceanographic Institution, MS#24, Woods Hole, Massachusetts 02543.

to land paleoseismic records, turbidite paleoseismology and other off-fault techniques must demonstrate that the events recorded are earthquake triggered, or provide a method to separate earthquakes from other signals in a mixed record. Marine records are commonly longer and more continuous than land records, and provided they are in settings isolated from the effects of sea level change, can actually be more precise in the early to mid Holocene due to the abundance of datable microfossils. In recent years, turbidite paleoseismology has been attempted in Cascadia (Adams, 1990; Nelson *et al.*, 2000; Goldfinger *et al.*, 2003a,b), Puget Sound (Karlin *et al.*, 2004), Japan (Inouchi *et al.*, 1996; Nakajima and Kanai, 2000; Shiki *et al.*, 2000), the Mediterranean (Kastens, 1984), the Dead Sea (Niemi and Ben-Avraham, 1994), northern California (Field, 1984; Garfield *et al.*, 1994), the southwest Iberian Margin (Garcia-Orellana *et al.*, 2006), Marmara Sea (Polonia *et al.*, 2004), and the Arctic Ocean (Grantz *et al.*, 1996) and is a technique that is evolving as a precise tool for seismotectonics.

In 1999, we collected 44 piston cores of 6–8-m length (Fig. 1) and 44 companion trigger cores of 2-m length and seven box cores ($50 \times 50 \times 50$ cm) in basin and channel systems throughout Cascadia basin to investigate the paleoseismic history of the Cascadia margin (Goldfinger *et al.*, 2003a). In 1999–2002, we collected 74 piston, gravity, and jumbo Kasten cores from channel/canyon systems draining the northern California margin adjacent to the onshore and nearshore NSAF (Goldfinger *et al.*, 2007; Fig. 2). During both cruises, we mapped channel systems with SeaBeam 2000 and Simrad EM-120 multibeam sonars, collecting both high-resolution bathymetry and backscatter data essential for analysis of channel morphology, sedimentation patterns, and core siting. These data were processed and merged with existing single and multibeam data to develop regional bathymetric datasets.

During these cruises, we sampled all major and many minor channel systems extending from Barclay Canyon off Vancouver Island to the Mendocino Triple Junction (MTJ) in 1999, and from Cape Mendocino to just north of Monterey Bay in 2002 (Figs. 1 and 2). In some cases, sampling both down and across channels was done and particular attention was paid to channel confluences, as these areas afford opportunities to test for synchronous triggering of turbidity currents.

These cores have yielded turbidite records that are in good agreement with the shorter land record of Holocene Cascadia and NSAF earthquakes (Goldfinger *et al.*, 2003a, b, 2007). While Cascadia has an extensive land paleoseismic record from numerous sites, a similar land paleoseismic record for the NSAF system has proven more difficult to establish, despite the intense scientific study of the NSAF stemming from the great seismic hazards to the San Francisco Bay Area. This is particularly true for the segments of the NSAF near and north of San Francisco that ruptured during the great 1906 earthquake.

In this article, we present results from the offshore turbidite event record along the NSAF extending to ~3000 yr B.P., with correlation evidence of the youngest events along strike that augments evidence presented in Goldfinger *et al.* (2007). We present new data from southern Cascadia, where a series of small correlatable marine turbidites and land evidence together suggest limited southern Oregon ruptures in addition to margin-wide ruptures. We then compare the NSAF temporal record to that of the combined land/marine Cascadia temporal record to explore a possible temporal and stress relationship between these two great plate boundary faults.

Geological Setting and Background

NSAF Seismotectonic Setting

The San Andreas fault (SAF) is probably the most intensively studied transform system in the world. Extending along the west coast of North America, from the Gulf of California to Cape Mendocino, the SAF is the largest component of a complex and wide plate boundary that extends eastward to encompass numerous other strike-slip fault strands and interactions with the Basin and Range extensional province. The Mendocino triple junction (MTJ) lies at the termination of the NSAF and has migrated northward since about 25–28 Ma (Dickinson and Snyder, 1979). As the triple junction moves, the former subduction forearc transitions to right-lateral transform motion, and the SAF continues to lengthen.

West of the Sierra Nevada block, three main fault systems accommodate ~75% of the Pacific–North America plate motion, distributed over an ~100-km-wide zone (Freymueller *et al.*, 1999; Argus and Gordon, 2001; d'Alessio *et al.*, 2005). Much of the remainder is carried by the eastern California shear zone (Sauber, *et al.*, 1994; Segall and Castillo, 1999). The NSAF accommodates about 25 mm/yr of the ~40 mm/yr distributed across western California. Most of the remainder is taken up on the parallel Hayward–Rodgers Creek system, and the slightly divergent Calaveras–Concord–Green Valley fault system farther to the east. The Hayward and Calaveras systems become the Maacama and Bartlett Springs faults, respectively, in northernmost California. South of San Francisco, the transform system includes the offshore San Gregorio fault, which joins the NSAF at Olema, just north of San Francisco. Between San Francisco and Cape Mendocino, the SAF is a relatively simple system with most strain localized on the primary strand. Several uncertain faults exist offshore, but the age and activity of these faults is unknown (Jennings, 1995). Seismicity offshore is virtually nil, with the exception of the MTJ region. Since the 1906 rupture, the main San Andreas has been nearly aseismic, with only a few small events near Point Arena (Zoback *et al.*, 1999). Seismicity has been greater on the Maacama and Bartlett Springs faults to the east (Castillo and Ellsworth, 1993).

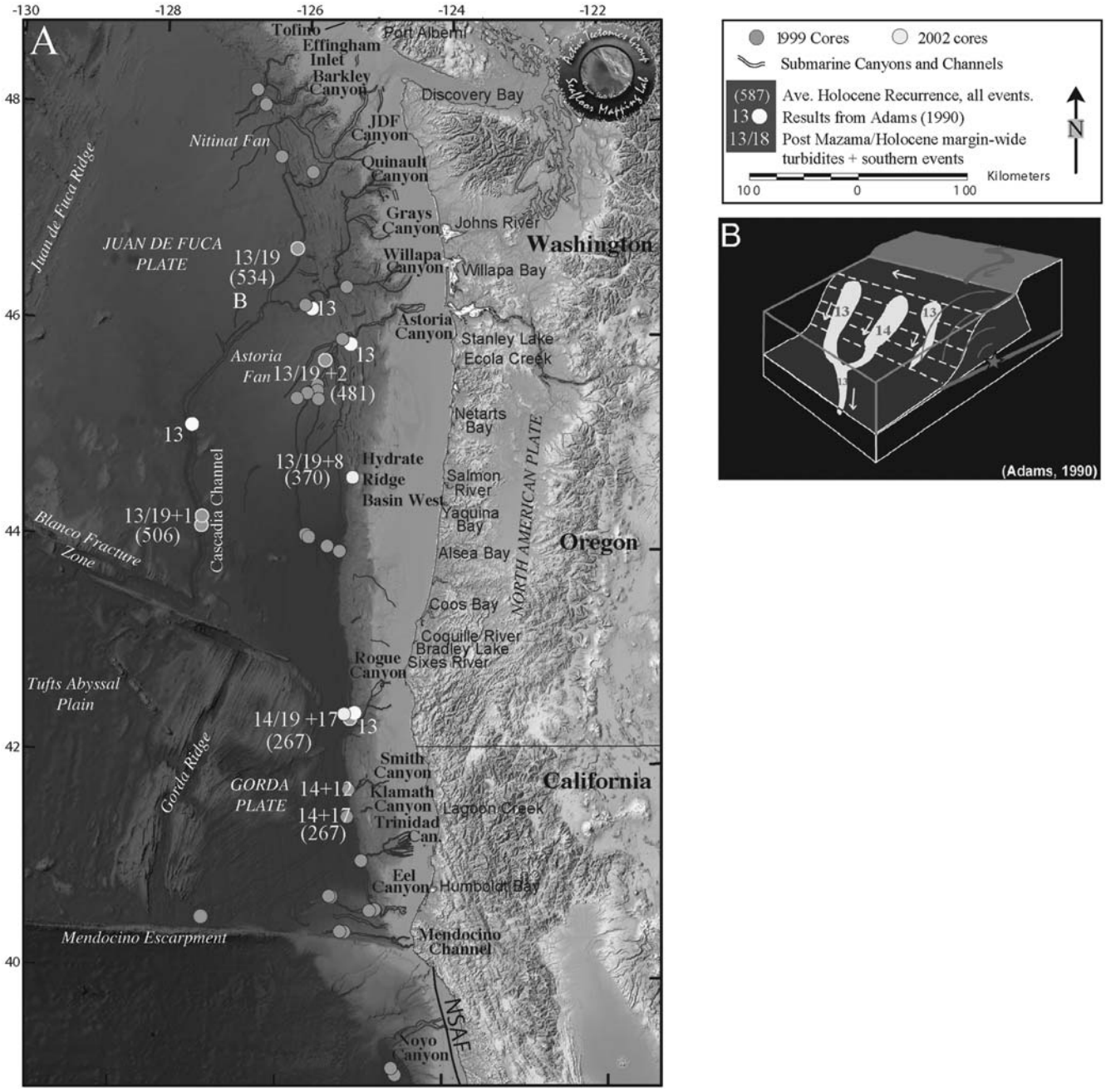

Figure 1. (a) Cascadia margin turbidite canyons, channels, and 1999–2002 core locations. The major canyon systems are outlined. Number of post-Mazama/Holocene correlative turbidites, with southern turbidites denoted with a +, are shown. Average Holocene recurrence times for all events are shown in parentheses. Mazama ash was not present in Barkley Canyon cores or in the cores south of Rogue Canyon. Primary core sites shown with light rim; other cores are gray. (b) Synchroneity test at a channel confluence as applied where Washington channels merge into the Cascadia Deep Sea Channel. The number of events downstream should be the sum of events in the tributaries, unless the turbidity currents were triggered simultaneously by an earthquake (Adams, 1990). This site is at B on the JDF plate.

The 1906 M_w 7.9 earthquake rupture extended from the epicenter near San Francisco north to Shelter Cove near Point Delgada and south to near San Juan Bautista, suggesting a minimum rupture length of ~470 km (Fig. 2). The 1906 event clearly ruptured the surface along the San Francisco peninsula to as far north as Point Arena (Lawson, 1908). Some debate exists regarding the full length of the 1906 rupture (McLaughlin *et al.*, 1983), though most investigators now believe the rupture extended to Point Delgada (Song *et al.*, 2008).

Offshore, numerous canyon/channel systems containing Holocene turbidites drain the northern California margin. From the north beginning at Cape Mendocino, to the south at Monterey Bay, the canyons and channels are Gorda,

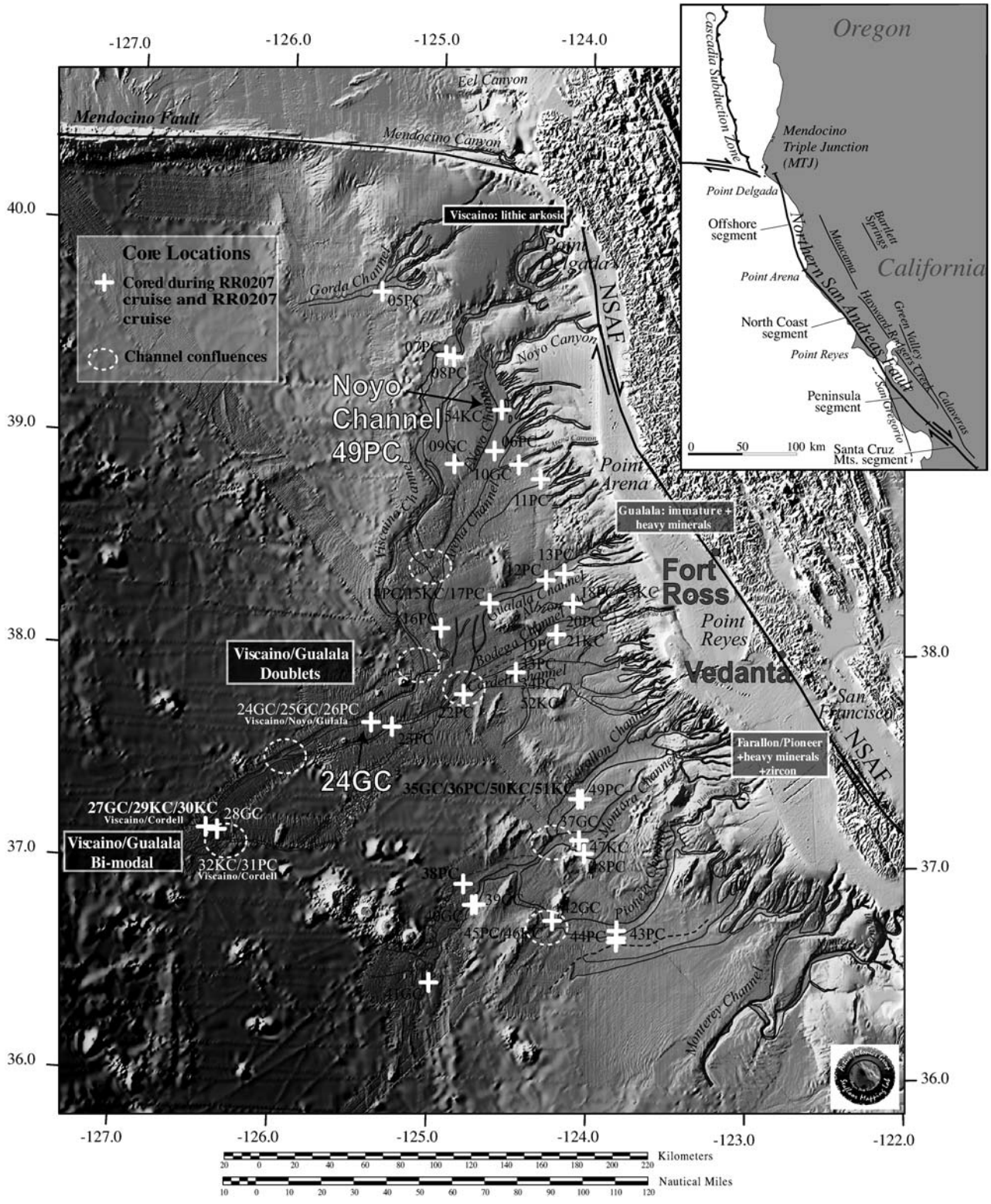

Figure 2. Core locations from 1999 and 2002 cruises on Research Vessel (R/V) Melville and R/V Roger Revelle along NSAF system. Bathymetric and topographic data compiled by Oregon State University (OSU) from archive and newly collected marine survey data during these cruises with NASA Shuttle Radar Topography Mission (SRTM) land data. Channel systems mapped from the new bathymetric grid and sidescan data. Core numbers are referred to in the text: piston core, PC; gravity core, GC; kasten core, KC; and box core, BC. Noyo Cores (including 49PC from Melville 1999 cruise) and 24GC, discussed in text, are also shown. Offshore provenance from heavy mineral analyses is indicated in boxed text. At the confluence upstream of core 24GC, Viscaino and Gualala mineralogies mix and result in stacked pulses, reflecting source mineralogies. Onshore paleoseismic sites Vedanta and Fort Ross are shown onshore.

Viscaino, Noyo, Arena, Gualala, Albion, Bodega Cordell, Farallon, Montara, Pioneer, and Monterey (Fig. 2). Some of these turbidite channels have downstream confluence pathways; for example, Noyo, Viscaino, and Gualala channels join together to form a single channel traveling hundreds of kilometers offshore. The Bodega, Cordell, and Viscaino turbidite systems behave in the same way along the southern half of the northern California margin meeting in another confluence (Goldfinger *et al.*, 2007). Confluences are important because they offer opportunities to test synchronous triggering of turbidity currents (Fig. 1b; Adams, 1990; Goldfinger *et al.*, 2003a, 2007).

Noyo Channel is found south of Cape Mendocino and extends seaward with a length of more than 200 km from the mouth of the canyon to the end of the pathway. The NSAF crosses the Noyo canyon head in ~150-m-water depth on the outer shelf, clearly offsetting the upper canyon head, which has also been captured by and bends 90° to follow the fault (Fig. 2). This makes Noyo canyon particularly sensitive to seismic activity on the NSAF. The Noyo turbidite record is therefore more robust than other channels that increase in distance from the fault southward to ~60 km south of Point Arena (Fig. 2).

Northern San Andreas Onshore Paleoseismicity

The NSAF system has been divided into segments based on its historical record of earthquake behavior. All four northern segments (north of the creeping section at San Juan Bautista, Santa Cruz Mountain, peninsula, north coast, and offshore; Working Group on California Earthquake Probabilities, 2003) ruptured in the 1906 M_w 7.9 earthquake, extending from San Juan Bautista north to the MTJ (Lawson, 1908; Brown, 1995; Thatcher *et al.*, 1997; Prentice *et al.*, 1999; Song *et al.*, 2008).

The onshore paleoseismology of the NSAF has been investigated at Olema, 45-km north of San Francisco; at Dogtown, close to the Olema site; at Bodega Bay, Bolinas Lagoon, Point Arena, and Fort Ross; and at several sites on the San Francisco peninsula and in the Santa Cruz mountains. At the Vedanta site (Fig. 2) near Olema, Niemi and Hall (1992) found a maximum late Holocene slip rate of 24 ± 3 mm/yr, in fair agreement with geodetic data (Segall, 2002; d'Alessio *et al.*, 2005). They estimate that if the 4–5-m slip event recorded in 1906 is characteristic, the recurrence time for such events would be 221 ± 40 yr. The average slip per event at Point Arena similarly implies a recurrence time of 200–400 yr (Prentice, 1989). Recently, 10 new ages from the Vedanta site (Zhang *et al.*, 2006) and sites near Fort Ross (Kelson *et al.*, 2006) (Fig. 2) suggest a recurrence interval of ~200 yr and timing of the penultimate event on the north coast and offshore segments at ~A.D. 1700–1750. Knudsen *et al.* (2002) document probable coseismic relative sea level changes within structural basins along the NSAF in Bodega harbor and Bolinas lagoon, 90 and 27-km north of San Francisco, respectively. These data suggest two events prior to 1906, one ~400 and another 700–750 yr B.P.

Cascadia Seismotectonic Setting

The Cascadia subduction zone is formed by the subduction of the oceanic Juan de Fuca and Gorda plates beneath the North American plate off the coast of northern California, Oregon, Washington, and Vancouver Island (Fig. 1). The Juan de Fuca–North America convergence rate decreases from 50 mm/yr at southern Vancouver Island to 36 mm/yr at the MTJ (poles of McCaffrey *et al.*, 2007). Juan de Fuca–North American convergence is oblique, with obliquity increasing southward along the margin. The submarine forearc widens from 60 km off southern Oregon to 150 km off the northern Olympic Peninsula of Washington, where the thick Pleistocene Astoria and Nitinat fans are presently being accreted to the margin (Fig. 1). The active accretionary thrust faults of the lower slope are characterized by mostly seaward-vergent thrusts on the Oregon margin from 42° to 44°55' N and north of 48°08' N off Vancouver Island, and by landward-vergent thrusts between 44°55' N and 48°08' N on the northern Oregon and Washington margins (Goldfinger *et al.*, 1997).

The earthquake potential of Cascadia has been the subject of major paradigm changes in recent years. First thought to be aseismic due to the lack of historic seismicity, great thickness of subducted sediments, and low uplift rates of marine terraces (Ando and Balazs, 1979), Cascadia is now thought capable of producing large subduction earthquakes on the basis of paleoseismic evidence (e.g., Atwater, 1987; Satake *et al.*, 1996; Atwater and Hemphill-Haley, 1997), geodetic evidence of elastic strain accumulation (e.g., Dragert *et al.*, 1994; McCaffrey *et al.*, 2000) and comparisons with other subduction zones (e.g., Heaton and Kanamori, 1984; Atwater, 1987). Despite the presence of abundant paleoseismologic evidence for rapid coastal subsidence and tsunamis, the plate boundary remains the quietest of all subduction zones, with only one major interplate thrust event ever recorded instrumentally (Oppenheimer *et al.*, 1993). Cascadia represents an end member of the world's subduction zones not only in seismic activity (Acharya, 1992) but also as the hottest subduction thrust because of its young subducting lithosphere and thick blanket of insulating sediments (McCaffrey, 1997).

Cascadia Paleoseismicity

The past occurrence of great earthquakes in Cascadia is now well established; thus, attention has turned to magnitude, recurrence intervals, and segmentation of the margin. Segmented and whole-margin ruptures should leave distinctly different stratigraphic records in both the coastal marshes and the offshore turbidite channel systems.

The most extensive paleoseismic record on land is found in subsided marshes and tsunami deposits of thin marine sand layers with diatoms that overlie marshes or are in-

terbedded within estuarine or lake muds (Atwater and Hemphill-Haley, 1997; Kelsey *et al.*, 2005; Nelson *et al.*, 2006; site localities shown in Fig. 1). The tsunami deposits are found several kilometers inland from the coast, up river estuaries, or in low-lying freshwater lakes near sea level but above the reach of storm surges. A 3500-yr record of such tsunami events and buried soils due to coseismic land subsidence is found in Willapa Bay, Washington (Atwater and Hemphill-Haley, 1997). In the coastal paleoseismic record, the average recurrence time of great earthquakes along the northern Cascadia subduction zone for the past 3500 yr (526 yr) (Atwater and Hemphill-Haley, 1997) agrees quite closely with the offshore average of 470 yr for the same period (one offshore event was not reported at Willapa Bay) and the 524-yr average over the 10,000-yr turbidite paleoseismic record (revised slightly from Goldfinger *et al.*, 2003a). Along the southern margin, an ~4600-yr record with 14 disturbance events likely from Cascadia subduction earthquakes has been carefully documented in Bradley Lake, on the southern Oregon coast (Kelsey *et al.*, 2005), along with a 5500-yr record at the Sixes River (Kelsey *et al.*, 2002). The Bradley lake record is the most complete land record on the southern margin and yields a shorter recurrence interval of 340 yr along that part of the southern margin. A compilation of southern Cascadia sites reported in Nelson *et al.* (2006) includes Bradley Lake and concludes that Cascadia has segmented ruptures along the southern margin in addition to full-margin ruptures.

Offshore, Cascadia Basin comprises the deep ocean floor over the Juan de Fuca and Gorda Plates, and extends from Vancouver Island, Canada, to the Mendocino Escarpment in northern California (Fig. 1). The Cascadia Basin contains a wide variety of Quaternary turbidite systems with an extensive Holocene history of turbidite deposition (i.e., Griggs and Kulm, 1970; Nelson, 1976). Recent work has documented the linkages between these turbidites and great earthquakes along the Cascadia subduction zone (Adams, 1990; Nelson *et al.*, 2000; Goldfinger *et al.*, 2003a,b).

The Holocene stratigraphy of submarine channels along the Cascadia margin includes Mazama Ash (MA), from the eruption of Mt. Mazama, forming Crater Lake, Oregon (Nelson *et al.*, 1968). The calendar age of the eruption of Mt. Mazama has recently been reevaluated with an age of 7627 ± 150 calendar years B.P. determined from the Greenland Ice Sheet Project (GISP) 2 ice core (Zdanowicz *et al.*, 1999). The Mt. Mazama eruption airfall was distributed northeastward from southern Oregon mainly over the Columbia drainage and some of the coastal rivers. It is also found in the Puget lowland, British Columbia (Hallett *et al.*, 1997), and in inlets on the west coast of Vancouver Island (Dallimore *et al.*, 2005). From these rivers, MA was transported to temporary depocenters in canyon heads of the Cascadia continental margin, much as Mt. St. Helens ash was transported following the 1980 eruption (Nelson *et al.*, 1988). Subsequent turbidity currents transported the ash into Cascadia Basin canyon and channel floor depocenters.

Using the MA marker bed, ^{14}C ages, and stratigraphic correlation, the offshore turbidite record has been demonstrated to be largely, if not entirely, composed of synchronous turbidites, 19 of which are margin wide and others that span shorter segments (Goldfinger, Morey, Erhardt, *et al.*, 2006). The synchroneity of the 10,000-yr turbidite event record along the northern half of the Cascadia subduction zone is best explained by paleoseismic triggering of great earthquakes with a mean recurrence interval for long ruptures of 496–524 yr, depending on the locality. Further refinement of the Cascadia record along the southern margin is discussed in the subsequent section.

Turbidite Methodology and Analytical Methods

Turbidite Methodology and Application to Cascadia and the San Andreas

Identifying Earthquake-Triggered Turbidites. An association between earthquakes and turbidity currents has long been known (Heezen and Ewing, 1952); however, other triggers for turbidity currents exist, including (1) storm or tsunami-wave loading, (2) sediment loading, and (3) storm (hyperpycnal) discharges, as well as less common occurrences such as bolide impacts and major subaerial or submarine landsliding. In some cases, seismic turbidites can be distinguished sedimentologically from storm, tsunami, and other deposits (Inouchi *et al.*, 1996; Nakajima and Kanai, 2000; Shiki *et al.*, 2000), although sedimentological distinction between triggering mechanisms may be somewhat site specific. We use synchronous triggering manifested as a spatial and temporal pattern of event correlations along both the Cascadia and NSAF margins to determine earthquake origin. Synchroneity of event records in separated canyons, over a wide region, is difficult to attribute to nonearthquake sources, which are most often limited spatially and temporally to single canyons. Possible exceptions could include storm or tsunami-wave loading and hyperpycnal flow, which can also occur over large areas and short time scales. These possibilities and the tests used to distinguish Cascadia and NSAF earthquake-generated turbidites from other triggering mechanisms have been presented in Goldfinger *et al.* (2003a, b, 2007) and Nelson *et al.* (2000).

Tests of Synchronous Triggering and Correlative Deposition of Turbidites. A key test of synchronous triggering has become known as the confluence test (Fig. 1b). In Cascadia Basin channels, Adams (1990) observed that most cores contained 13 turbidites overlying the MA (which was included in the thirteenth). Cores from Juan de Fuca Canyon, Willapa, Grays, and Quinault Canyons also contain 13 turbidites and include the MA. The correlative turbidites in Cascadia channel lie downstream of the confluence of those channels. If these events had been independently triggered, with more than a few hours separation in time the channels below, the confluence should contain 26 turbidites, not 13 as observed. This simple observation demonstrates synchronous trigger-

ing of turbidity currents in tributaries whose headwaters are separated by 50–150 km (Fig. 1b). In our Cascadia work, we find that all of the northern Cascadia events that traverse the Willapa–Juan de Fuca Channel confluence pass this test, a total of 19 events including the 6 that lie below the MA. These events pass this test with more precision than simply the number of events upstream and downstream. The events are all composed of 1-to-3 coarse sand pulses with characteristic grain-size distribution, and this structure or event fingerprint is also preserved above and below the confluences, a phenomenon further discussed next.

We also applied a confluence test to the NSAF turbidite data as they pass through six confluences, and we modify the test to include the mineralogic fingerprinting of the input channels during an ~6000-yr period. We broadly distinguish three heavy mineral provenances in the NSAF cores, well linked to the onshore source geology (Figs. 2 and 3). Using these three heavy mineral suites allows us to distinguish the various dominant tributary canyon sources of the stratigraphy within turbidites, both up- and downstream from confluences. With this mineralogic test for synchronous or asynchronous arrival of individual coarse fraction pulses, we can correlate the stacking of these pulses and associated provenance components to establish or refute synchronous triggering. Further details of confluence tests applied to NSAF margin cores are presented in Goldfinger *et al.* (2007).

Analytical Methods

Stratigraphic Correlation and Event Fingerprinting. While at sea, all cores were scanned using a GEOTEK Multi-Sensor Core Logger (MSCL), collecting *P*-wave velocity, gamma-ray density, and relatively coarse magnetic susceptibility data using a loop sensor from the unsplit cores. Cores were then split to collect high-resolution line-scan imagery. Subsequently, high-resolution magnetic susceptibility data were collected from each core using a point probe (Bartington MS2E high-resolution surface sensor) at 1-cm intervals and imaged with *X* radiography (Figs. 3–6). For the upper-

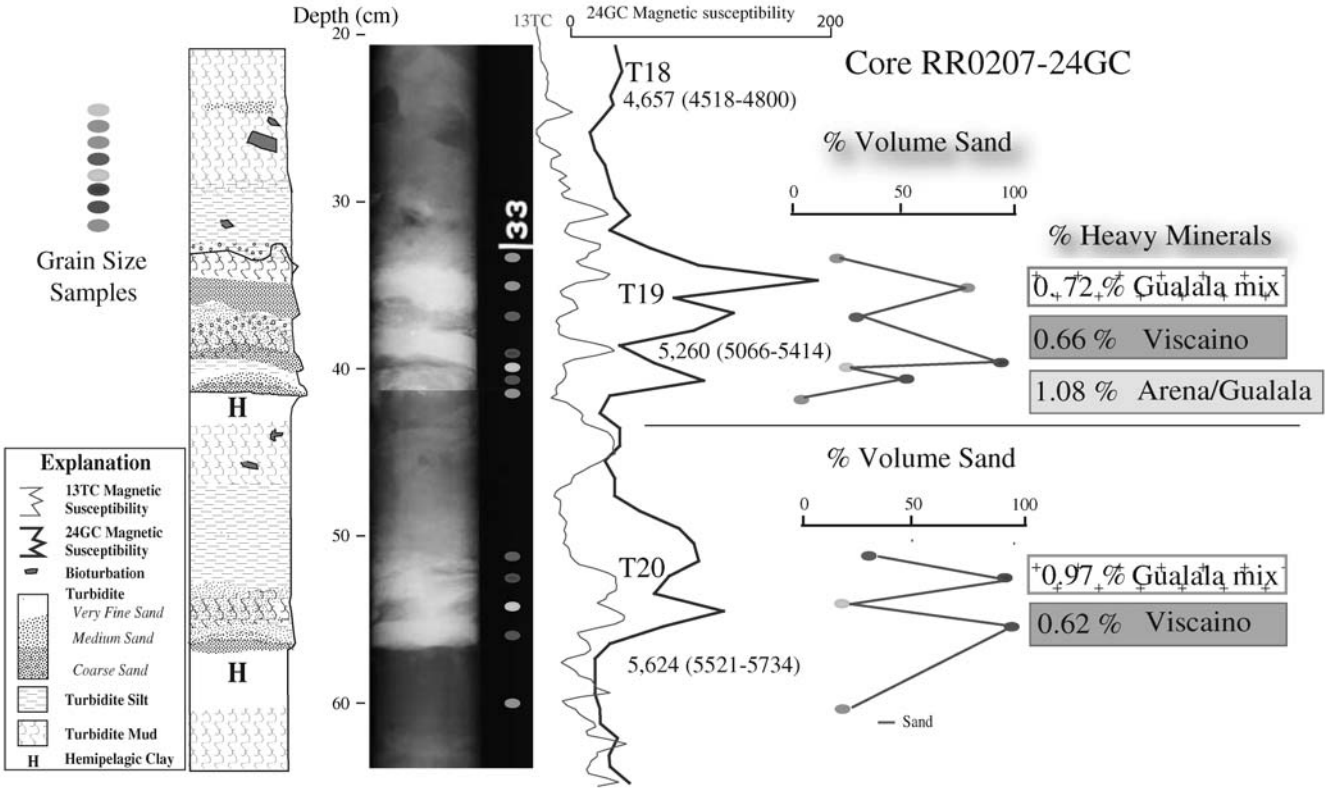

Figure 3. Example grain size analysis, magnetic susceptibility/density signatures and *x*-radiography in turbidites T19 and T20 in core 24GC below the Gualala–Noyo–Viscaino channel confluence (base of T18 is also shown; see Fig. 2 for location). Light tones in the *x*-radiograph represent dense sand/silt intervals; darker gray tones represent clay/mud. Oval dots are grain size samples. Heavy trace is the magnetic susceptibility signature. Right plot is percent sand (obtained with Coulter laser counter method). The good correspondence between grain size, density, and magnetic susceptibility for the lithologies in both Cascadia and NSAF cores is established with selected analyses, and permits use of density and magnetics as mass/grain size proxies that show much greater resolution than possible with grain size analysis. These typical turbidites are composed of 1-3 fining-upward sequences, each truncated by the overlying pulse. No hemipelagic exists between pulses, indicating the three pulses were deposited in a short time interval. Only the last pulse has a fine tail, indicating final waning of the turbidity current. We interpret these signatures as resulting from a single multipulse turbidity current. Number of coarse pulses commonly remains constant in multiple channel systems for a given event. Source provenance affinity for each sand pulse is shown to the right, and keyed to source regions in Figure 2.

most ~1 m, cores along the base of the continental slope along the NSAF were further sampled using point magnetics at a 3 mm spacing to compensate for a low latest Holocene sedimentation rate in those cores. Selected grain-size analyses for both regions were performed with a Coulter laser counter.

Cores were scanned using a GEOSCAN line-scan system using a 3 × 1024-pixel charge-coupled device at 1-mm resolution. Color reflectance data (red, green, blue [RGB] traces) were extracted from the high-resolution imagery by averaging a 100-pixel swath across the core for each data point, and these were compiled down the core. Color reflectance is a common high-resolution physical property, which is useful when the stratigraphy has enough color contrast to be diagnostic of stratigraphic detail (Nederbragt *et al.*, 2006; Rogerson *et al.*, 2006). Unlike the other physical property measurements, color reflectance is highly influenced by the surface condition of the split core. Irregularities due to core splitting, smoothing of the core surface, water content, and other factors can influence the color data. Interpretation of the color data thus must be done when directly overlain on the color core imagery so as to remove such artifacts from consideration. Extraction of the RGB data from the imagery was done to best avoid these artifacts. While color reflectance has been commonly used to estimate chemical content, particularly of CaCO3 (i.e., Lyle *et al.*, 2002), and hyperspectral imagery can extend this capability, we here use color reflectance for detecting the light–dark pattern resulting from alternating fine-grained mud turbidites (dark) and interbedded hemipelagic intervals (light).

Turbidite correlation is done using primarily magnetic susceptibility and density, much as e-logs are correlated in the oil industry (McCubbin, 1982; Lovlie and van Veen, 1995). Physical property correlations of this type are also common practice with academic and ocean drilling program/integrated ocean drilling program (ODP/IODP) cores (e.g., Fukuma, 1998) and have recently come into use for paleoseismology (i.e., Schnellman *et al.*, 2002; Abdelayem *et al.*, 2004; Goldfinger, Nelson, Johnson, Arsenault, *et al.*, 2004; Hagstrum *et al.*, 2004; Iwaki *et al.*, 2004; Karlin *et al.*, 2004; St-Onge *et al.*, 2004; Goldfinger *et al.*, 2007).

In addition to local site correlation, we have found that it is possible to correlate unique physical property signatures of individual turbidites from different sites within individual channels. This suggests that the processes controlling deposition of the turbidite maintain consistency for some considerable distance within a channel. We have also found it possible to correlate event signatures not only down individual channels and past confluences, but between channel systems separated by considerable distance, some of which never meet. These turbidite fingerprints form the basis of long-distance correlations and are beginning to be recognized and used for regional correlation (e.g., Lake Baikal, Lees *et al.*, 1998; off Morocco, Wynn *et al.*, 2002; Cascadia, Goldfinger, Nelson, Johnson, and Morey, 2003; the Laptev Sea: Russian Arctic, Rivera *et al.*, 2006; and elsewhere). Recently, the event signatures of Cascadia turbidites have been linked to coastal fjord records on Vancouver Island (Dallimore *et al.*, 2005; Goldfinger, Morey, Erhardt, *et al.*, 2006).

Figure 3 shows a single representative turbidite in core 24GC, located below two channel confluences, that illustrates the multiple fining-upward sequences (Bouma A–C) that compose each turbidite. Typically, these sequences have only one fine tail (Bouma D) associated with waning of the turbidity current. The signatures we are correlating are comprised of these stacked coarse pulses. This figure shows in detail that the magnetic susceptibility, density, and grain size trends within each event are closely correlated. This is straightforward but important because we can, in most cases, use the high-resolution density and magnetic data as grain size proxies, at least for lithologies along the Cascadia and NSAF systems (Goldfinger, Nelson, Johnson, and Morey, 2003; Morey *et al.*, 2003; Wynn and Masson, 2003). Further details of the use of magnetics and density as grain size proxies are given in Goldfinger *et al.* (2007).

On close inspection of physical property logs, we sometimes see a remarkable similarity between correlative turbidites that are separated by as much as 500 km (Cascadia) and 280 km (NSAF). Figure 4 shows several typical examples of correlative events over a distance of 470 km along the Cascadia margin. We see a general correspondence of relative turbidite thickness downcore that is reflected in separate channels, as well as correlable details such as the number of coarse sandy pulses (density and magnetic peaks).

For example, Cascadia turbidite events T2, T10, and T12 are small events in all cores, whereas T11 and T16 are very large events in all cores, and many other events follow similar size patterns across both Cascadia and the NSAF margins. Vertical sequences of turbidite size and number of pulses are commonly preserved between remote sites, and were used to aid in the correlation framework. We observe similar patterns along the NSAF margin, where size trends and individual characteristics persist over large distances. Goldfinger *et al.* (2007) also show the evolution of a single event down channel over a distance of 74 km, showing the gradual merging of two sand pulses into a bimodal grain distribution. Stratigraphic correlation has the potential to establish links of individual events between core sites, independent of radiocarbon ages. Possible explanations for the correlation signatures are discussed in the following sections.

Radiocarbon Analysis. To date the turbidites, we extract Planktic foraminifers from the hemipelagic sediment below each turbidite. We do this because the boundary between the top of the turbidite tail and the hemipelagic sediment is difficult to identify, and bioturbation is concentrated at this boundary, possibly because the organic material brought down in the turbidite tail results in a benthic bloom (Smith *et al.*, 1993). Sensitivity tests for species-specific biases are presented in Goldfinger *et al.* (2007), as are the methods used to evaluate basal erosion. The close match and lack of consistent bias in ages between land and marine events observed

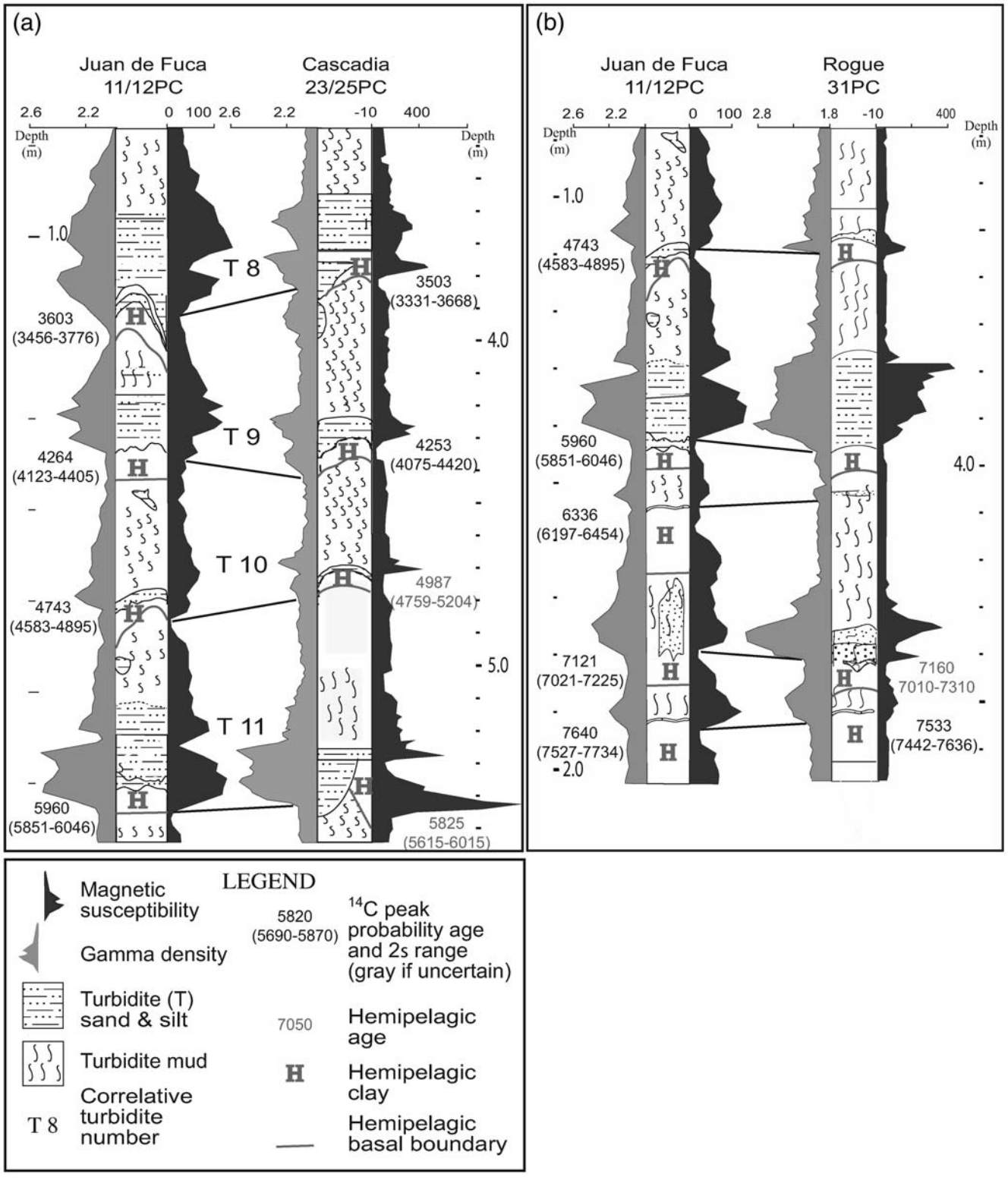

Figure 4. Correlation details from two representative pairs of cores on the Cascadia margin. (a) Events 8–11 in cores from Juan de Fuca Channel (left) and Cascadia Channel (right). Left traces are raw gamma density; right traces are magnetic susceptibility. Lithologic logs are also shown. The vertical scale is core depth in meters. Note correspondence of size, spacing, number of peaks, trends between events, and shape of physical property traces between these cores. (b) Events 10–14 in Juan de Fuca Channel (left) and Rogue Channel (right). In (a) cores are part of the same channel system; distance is 475 km. In (b) cores are in channels that do not meet; distance is 500 km. These are representative of full-margin events that are included in the southern margin correlation of Figure 6. Full correlation details presented in Goldfinger, Morey, Erhardt, *et al.* (2006a) and C. Goldfinger *et al.*, unpublished manuscript, 2007).

in both Cascadia and on the NSAF also suggests that neither bioturbation (Wheatcroft, 1992; Thomson *et al.*, 1995) nor basal erosion significantly bias ^{14}C ages derived from Planktic foraminifers in most cases. In several cases for Trinidad, Smith, and Klamath Channels, we dated benthic forams where Planktic foraminifers were not abundant enough to obtain a result. These ages were calibrated using the additional reservoir difference between benthic and planktic samples established locally for those cores in the 0–3000-yr time range. This method is similar to that used to establish the modern reservoir value (e.g., Hughen *et al.*, 2004).

Using a moving window average sedimentation rate, we corrected the original AMS ages for the radiocarbon sample thickness by subtracting the time corresponding to the thickness of the sample interval. Hemipelagic thickness was then converted to time for input into OxCal calibration software using the Marine04 database (Ramsey, 1995; Ramsey, 2001; Reimer *et al.*, 2004). A sedimentation-rate regression analysis was employed to flag erosion at a given interval and to provide a check for consistency downcore, as sudden hemipelagic sedimentation-rate changes in the marine environment are relatively rare (Ⓔ see the electronic edition of *BSSA*). Outliers in this analysis are most likely caused by basal erosion because ages appear to be older, with less sediment thickness between events than expected. To evaluate flagged outliers, we tested them for basal erosion by comparing the hemipelagic thickness of that interval among several closely spaced cores. In a few cases, multiple cores revealed that these anomalous intervals were the result of basal erosion on the core from which the sample was taken, based on a thinner hemipelagic section in only that core. If the dated interval was found to wholly or partially come from an interval suspected of erosion, and other dating options were exhausted, we calculated a corrected age based on the full hemipelagic thickness represented in the nearby cores. This correction applies to four samples in this study; Ⓔ the calculations and criteria are given in Table 2 in the electronic edition of *BSSA*. If more than one sample was used for the anomalous age, the correction was weighted by the proportion of the sample weights. See Gutierrez-Pastor *et al.* (2007) for a full discussion of these methods. To verify this type of correction, or to calculate the age of an undated turbidite, we can additionally calculate the age of the turbidite based on a dated turbidite below or above (or both if possible) the suspect/missing turbidite. The reference age above or below must be well dated at the suspect site and at other nearby sites to provide a stable reference. We can then calculate the age of the suspect event by adding the hemipelagic time to or subtracting it from the reference age to establish a calculated age for the event. This can also be done with OxCal, though the Bayesian calculation actually provides weaker constraints than those of the analytical solution using the full hemipelagic time constraint. We have included ages corrected by these methods where the erosion correction and the calculated age methods produce similar results (significant overlap at the 1-sigma level). These are indicated as such in the tables and figures, with calculations given in Ⓔ Table 2 of the electronic edition of *BSSA*.

Goldfinger *et al.* (2007) illustrate use of OxCal to take advantage of multiple ages (if within analytical error of one another), including constraints imposed by the time represented by hemipelagic sediment between events. In one case (the penultimate NSAF event) we used the establishment of the first San Francisco mission in 1769 to restrict the age. Where age data are missing, sedimentation rates alone can be used to model event ages, which we have done for several events in our time series due to scarcity of foraminifers in those intervals. Ⓔ Figure 1 in the electronic edition of *BSSA* shows the analyses for the A.D. 1906 and the penultimate NSAF events, as well as the A.D. 1700 Cascadia event using OxCal with hemipelagic sedimentation and historical constraints. Using these well-known events, and time constraints provided by the hemipelagic sediment deposited in the interseismic period, OxCal returns the calendar age of the A.D. 1906 NSAF and A.D. 1700 Cascadia earthquakes to within a few years. The penultimate event is similarly constrained to a narrower time window than obtained by simple calibration. Further details of the OxCal analysis and the reservoir corrections applied are given in Goldfinger *et al.* (2007). Also of importance here is the significance of the probability peaks in the probability density functions (PDFs). Multiple peaks and broad distributions in the PDFs are generated largely from the slope of the atmospheric radiocarbon curves, and without other data, can only be treated statistically. For marine data in this study, we have both hemipelagic intervals that represent the time elapsed between turbidites, and sedimentation-rate curves that serve to further constrain the time of emplacement. The hemipelagic intervals represent time during which earthquakes are precluded and restrict the time intervals in which earthquakes could have occurred. Similarly, sedimentation rates derived from multiple cores at a site can be used to show that most events occur near the probability peaks, eliminating much of the probability tail and additional peaks in the case of multiples. Our data show that marine sedimentation rates vary little, and can be used in this setting to support the use of probability peaks as shown by Goslar *et al.* (2005). Ⓔ We show the NSAF PDFs and rate curve fit in Figure 2 in the electronic edition of *BSSA*. This method presently cannot be used in Cascadia because no individual site has a record with all or nearly all events dated.

Heavy Mineral Analysis. Broad provenance bins were determined from standard heavy-mineral analysis techniques. We sieved samples of coarse material from the sand fraction of selected turbidites, and separated the heavy minerals with tetrabromoethane (specific gravity is 2.9), separating light and heavy fractions. We then made grain mounts of the heavy mineral fraction with piccolyte (refractive index is 1.52) and point counted at least 300 grains, 200 being true heavy minerals.

Results: Southern Cascadia and Northern San Andreas Turbidite Record

Southern Cascadia Event Correlation

Stratigraphic Correlation. The ^{14}C age framework and stratigraphic correlation of Cascadia margin turbidites, supported by extensive onshore paleoseismic work, allow a relatively complete Holocene assessment of rupture lengths and timing of Cascadia events. A full documentation of the combined onshore/offshore analysis is presented in C. Goldfinger *et al.* (unpublished manuscript, 2007). In this article (Ⓔ and in the electronic edition of *BSSA*), we present a subset of the Cascadia data and analyses focusing on the southern Cascadia margin during the past ~3000 yr in order to make comparisons between the southern Cascadia and NSAF time series.

The southern Cascadia margin has a paleoseismic record both onshore and offshore that differs from the record of the northern margin. Kelsey *et al.* (2005) and Nelson *et al.* (2006) present evidence for segmentation of the southern Cascadia margin. Our offshore record from southern Cascadia also suggests segmentation not initially recognized in Goldfinger *et al.* (2003a,b) and similar to that proposed by Kelsey *et al.* (2005) and Nelson *et al.* (2006). We now recognize 19 paleoseismic turbidites correlated along the northern 2/3 of the Cascadia margin, one more than reported previously because one event was discovered to be a closely spaced couplet. All 19 events were originally correlated to Rogue Canyon. We now find that most of these events can be correlated southward to Klamath, Smith, and Trinidad Canyons (younger than 4000 yr) off northern California as well. We find evidence of additional events along the southern margin, some of which appear to extend north to Central Oregon, and others that extend approximately to the Rogue site only, involving northern California and southern Oregon. These events are smaller muddy turbidites that can be observed as magnetic and density signatures between the larger margin-wide events. These small events are also noted in the original core logs as darker intervals within what was initially logged as hemipelagic sediment between major turbidites. The origin of the darker intervals was initially unknown; however, we now interpret these darker intervals as fine-grained mud turbidites on the basis of stratigraphic correlation between sites, and more detailed lithologic examination. An example, event T2a, is shown in Figure 5 (we retain the original 18 event numbers to maintain consistency with

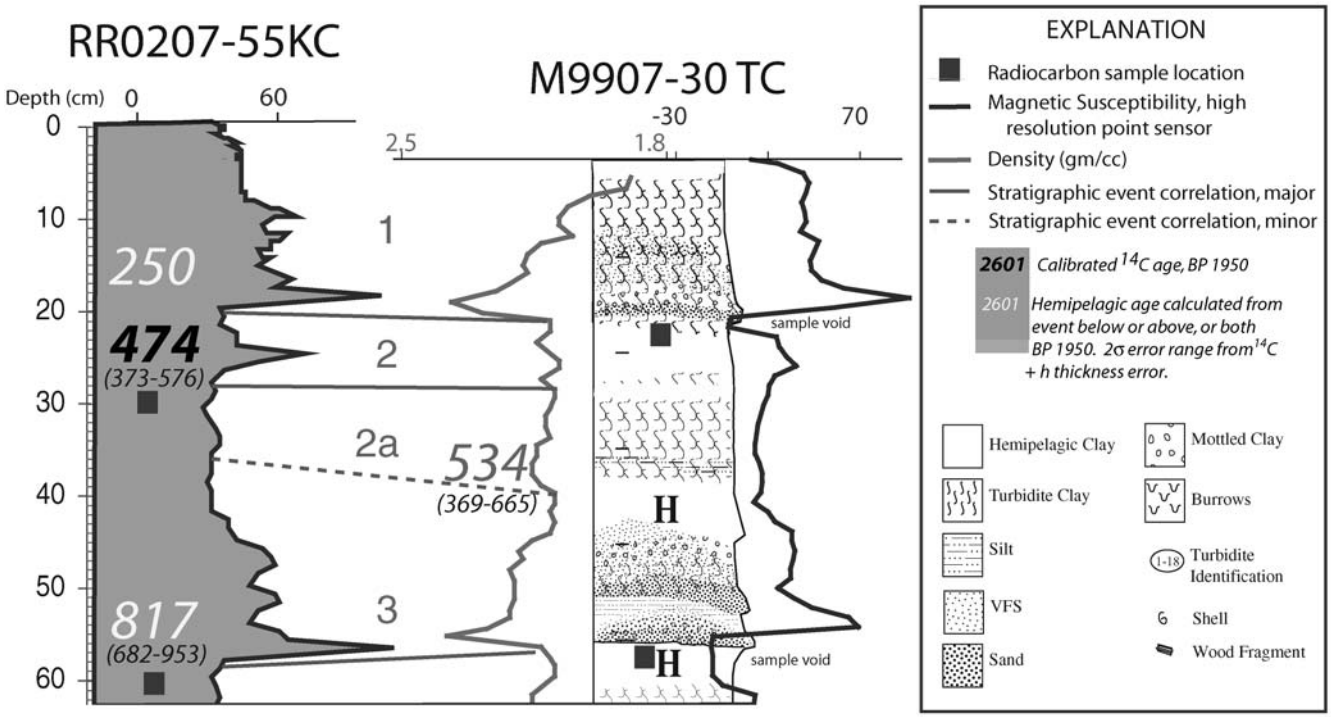

Figure 5. Grain size distribution for small southern event T2a. This event is representative of the smallest of the southern Oregon events correlated in this study. Detailed magnetic susceptibility and Gamma density records reveal a minor event between T2 and T3, which was originally logged as darker clay thought to be hemipelagic material. Closer inspection revealed this silt stringers and turbidite mud at this interval and also for T3a, T4a, T5a, T5b, and T6a. Similarity of small event grain size patterns between cores (magnetic susceptibility and density proxies), consistent appearance at the same intervals in multiple cores, and the observed silt/turbidite mud stringers supports interpretation of them as small mud/silt turbidites. Lithologic detail is composited from cores 55KC, 30TC, and 31TC. The vertical scale is core depth in centimeters. Ages calculated from adjacent ^{14}C ages shown with errors propagated from the radiocarbon age and the estimated error range for hemipelagic thickness. T1 (A.D. 1700 is 250 B.P. 1950) age assumed, not dated in this core. Regional correlation including this event is shown in Figure 6.

earlier publications, and insert smaller southern Cascadia events as a–c designations between margin-wide events in this study). Some of these weak events are not presently datable by ^{14}C methods, and for these events we have calculated their ages based on hemipelagic intervals above or below well-dated larger events as described previously.

Figure 6 shows stratigraphic correlation and ^{14}C ages for the Cascadia margin for the period 0–3000 yr B.P. Stratigraphic correlation of events is particularly good for the northern margin, with no events uncorrelated (i.e., appear in only one or two systems). For the northern margin, all events pass a strict synchroneity test, as they are found both above and below the confluence of Willapa and Juan de Fuca Channels with no change in number of events above (or below) the Mazama ash datum. This synchroneity test is critical to the establishment of synchronous triggering, and thus to the establishment of earthquake origin. Further discussion of Cascadia and NSAF synchroneity tests can be found in Adams (1990), Goldfinger *et al.* (2003a,b), and C. Goldfinger *et al.* (unpublished manuscript, 2007). Stratigraphic correlation as shown in Figure 6 illustrates the recognizeable fingerprints for individual events, which also can be observed on both sides of the Willapa–Juan de Fuca (JDF) confluence. This indicates that not only are individual turbidity currents merging to form one at the channel confluence, but that the fingerprints of individual events are preserved, im-

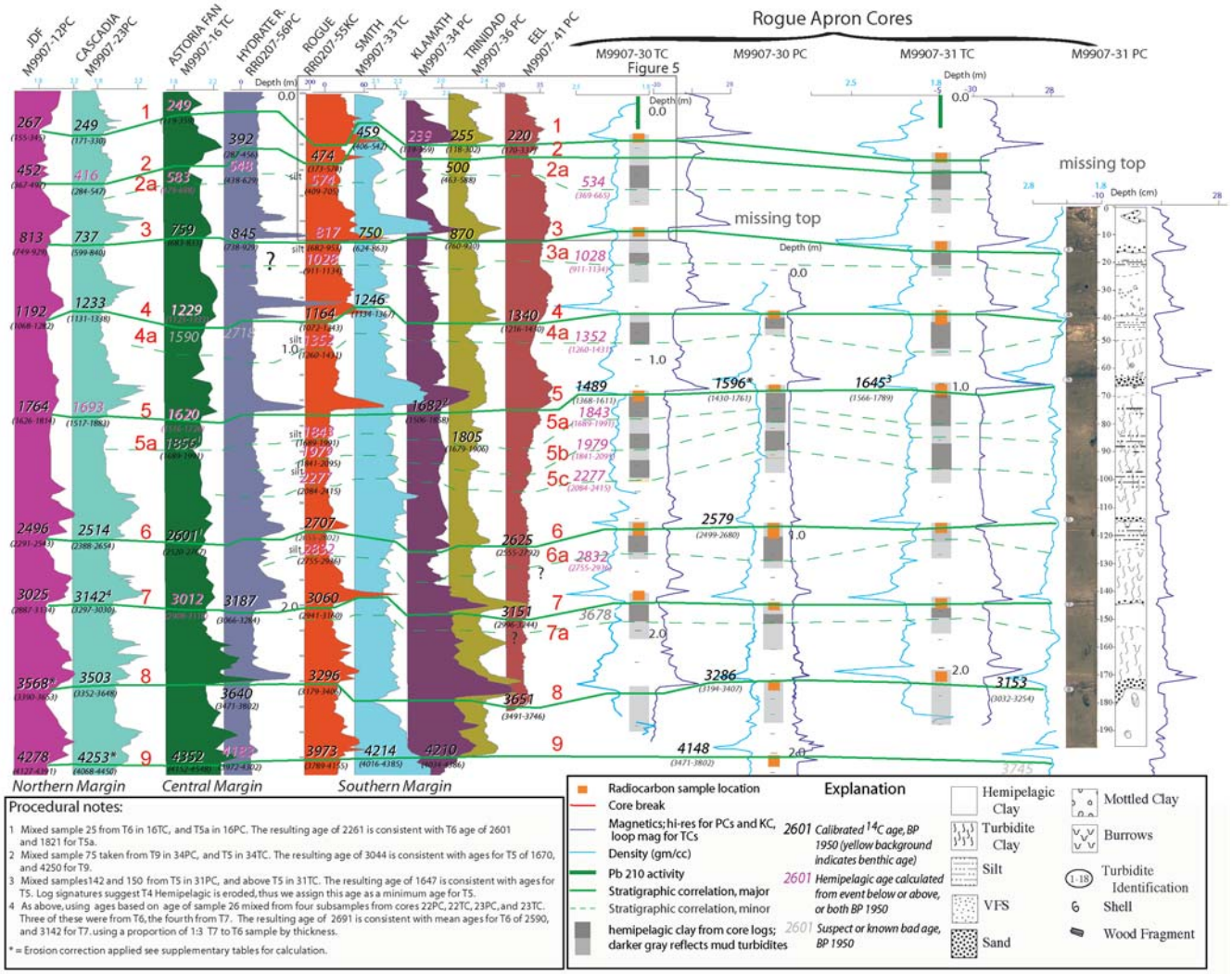

Figure 6. Correlation plot of marine turbidite core records and ^{14}C ages along the Cascadia margin from the JDF Channel to Eel Channel for the most recent ~4200 yr. Stratigraphic correlation allows resolution of some of the ambiguities pointed out by Nelson *et al.* (2006) for Southern Cascadia events. Event ages are shown using probability peaks from OxCal calibrations and combines where multiple ages at a site are available. See Figure 9 for PDFs for these ages. Events and sites linked by stratigraphic correlations are shown by connecting lines. Full-margin events correlated using stratigraphy and ^{14}C are shown thicker; local southern Cascadia events are thinner and dashed. The vertical scales for all cores are hung on the vertical scale of the Rogue cores, which are shown in expanded detail at the right. Relatively sparse dating of southernmost cores reflects low abundance of forams and thin hemipelagic intervals. Margin-wide event correlation represented by Juan de Fuca and Cascadia channel cores shown at left. Ages modified after Goldfinger *et al.* (2003a,b), Johnson (2004), and Gutierrez-Pastor *et al.* (2007) using additional data and analyses. Data in Figure 5 outlined by gray box.

plying that they were similar above and below the confluence. This further constrains the timing and increases the significance of the stratigraphic correlations in that the structure of the multipulse turbidity current that deposited the multipulse turbidite must have been similar in separate channels above the confluence, and must have survived the merging at the confluence.

Cascadia Time-Stratigraphic Event Correlation. Figure 7 shows a space-time diagram for the Cascadia margin for the past ~3000 yr, including the land and marine data used in this study as well as land data not included in the tabular age calculations. Ⓔ These data are also found in Tables 1–3 in the electronic edition of *BSSA*. This figure shows the time series of major Cascadia margin events interpreted as earthquakes recorded both onshore and offshore. The onshore events have been subjected to rigorous tests of earthquake origin that typically comprise rapid subsidence and sudden burial of marsh surfaces with tsunami sand. Details of the tests applied to individual sites are contained in the original literature. We favor the most recent work in which these tests and sampling methods are more robust than in the earlier works, and favor sites that have multiple well-constrained ages for each event, and ages that use seeds and needles over those that use peat-plant material. Event records vary somewhat in their preservation of events and in natural variability that comes from segmented margin ruptures. For events interpreted to be full-margin events based on the joint land/marine data, we use the best ages from sites along the margin to constrain event ages. For southern Cascadia events, we follow Kelsey *et al.* (2005) and Nelson *et al.* (2006) in attempting to clarify segmented ruptures through addition of the marine turbidite record.

The total number of events in the 3000-yr time range of this study, whether onshore or offshore, is similar, with a few differences noted here. The correspondence between offshore and onshore events in time is also striking. We suggest that the smaller events recorded offshore are in some cases the same events recorded onshore, though we cannot with certainty demonstrate this link. Some of the smallest events offshore likewise are represented by a spotty or absent record onshore. While this reduces our confidence in these events, it is also consistent with smaller earthquakes leaving a more discontinuous geologic record. We also note that the smaller turbidites offshore correspond reasonably well to the local southern Oregon events where they have been dated. In some cases, these turbidites cannot be dated directly, but have hemipelagic ages similar to onshore earthquakes, and lie in time ranges constrained by bracketing turbidite ages that also have corresponding onshore earthquakes. These earthquakes have limited rupture length in both onshore and offshore records, suggesting a first-order compatibility between offshore turbidite size, shaking intensity or duration (controlling turbidite volume), and rupture length. The offshore rupture limits reflected in the Figure 6 correlation are derived

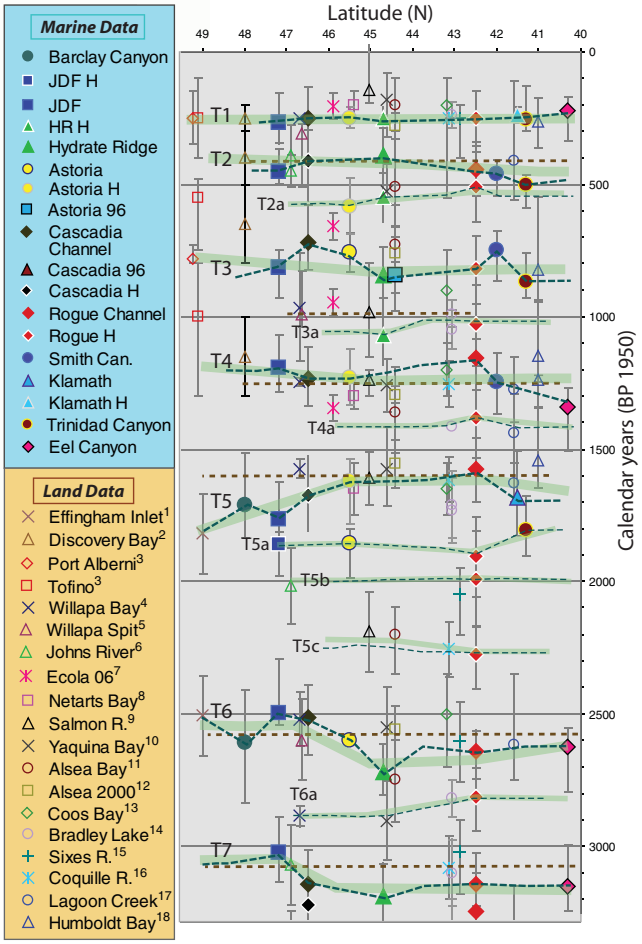

Figure 7. Space-time diagram for the Cascadia margin showing land and marine data for the past ~3300 yr. Filled symbols are marine turbidite data; open symbols are land paleoseismic data. Blue dashed lines show stratigraphic correlation of the turbidite data. Smaller southern Cascadia events are shown with thinner dashed lines. Site localities shown by symbology; locations shown on Figure 1. Marine symbols surrounded by white border are ages calculated from events above, below, or both using hemipelagic thickness and sedimentation rates. Green bars are best-fitting marine age trends for Cascadia earthquakes. Marine trends show space and time variant trends in some locations and time ranges due to reservoir age variability, further discussed in text. Best-fitting combined land/marine trends shown in brown dashed lines where reservoir effect is apparent. Ⓔ Land data and numbered sources and marine data are in Tables 1 and 2 of the electronic edition of *BSSA*, respectively.

from our interpretation of the combined land/marine data shown in Figure 7.

Offshore, the turbidite record gives a positive stratigraphic method of determining rupture length, limited by the uncertainty in triggering distance between canyons (estimated to be less than 90 km for full-margin events, and almost certainly less for smaller events, Goldfinger *et al.*, 2007) and uncertainties in correlation. ^{14}C ages for offshore events also provide constraints on rupture lengths. Onshore, the constraints are weaker because individual events cannot be correlated directly. The links between onshore events are thus mostly based on ^{14}C with some additional constraints

from the stratigraphic sequences at the land sites. In no cases do we find land events extending beyond the latitude limits of the marine record. In most cases, latitude limits are similar, but in a few cases, such as T2, the marine correlatives extend to greater latitude limits. Several of the smaller events in the marine record apparently have no land equivalents (T2a and T6a). These are the smallest of the marine events, with narrow latitude limits; thus, we suggest that the marine record is likely more sensitive to these small events. Limited rupture lengths and presumably magnitudes for these events may lack sufficient stress drop to generate significant tsunami or land subsidence, though they apparently do generate small correlatable marine turbidites. Alternatively, these small offshore events may not correlate as we infer, and would then be uncorrelated local events of no significance in the marine earthquake record. Although the correlation evidence and limited ^{14}C ages for these events make them less robust than the larger events, their appearance at the same intervals in numerous cores from isolated environments in Cascadia basin channels and slope basin cores makes such a coincidence unlikely.

Cascadia Rupture Modes. From the combined land/marine stratigraphic and radiocarbon data, we infer that in contrast to the northern margin, the southern Cascadia margin records a total of 38 probable earthquakes (10,000-yr record, Goldfinger, Morey, and Nelson, 2006) that are correlated between multiple sites, and thus define a mean recurrence interval for the southern Cascadia margin of ~260 yr in the Holocene, and a recurrence interval of 215 yr during the ~3000-yr period considered in this study. The combined stratigraphic correlations, hemipelagic analysis, and ^{14}C framework represented in the correlation figures, the space-time-diagram, and the supplementary tables can be summarized in Figure 8, which shows groupings of rupture lengths supported by the combined onshore and offshore records. We show the most recent 3000-yr period relevant to this article. For this 3000-yr interval, and considering the uncertainties in the southern rupture limit, we consider four rupture lengths as shown in Figure 8, which include the event numbers as shown in Figures 6 and 7 corresponding to the four modes. Overall, the Holocene record suggests that the Cascadia margin effectively has five rupture modes (refined from the four shown in Goldfinger, Morey, Erhardt, *et al.* [2006]): 19 full- or nearly full-length ruptures (50%), 2 ruptures comprising the central and southern half of the margin (5%), and 17 smaller southern margin ruptures that have three general groupings of rupture length (45%) during the Holocene. The southern limits of each rupture are not as well constrained as the northern limits; thus, rupture mode D could include other events, or may be the same as mode C. Interestingly, the northern limits of the shorter southern ruptures appear to terminate at three major structural uplifts known as Nehalem, Heceta, and Coquille Banks. Brudzinski and Allen (2007) have recently suggested that episodic tremor and slip (ETS) events downdip on the subduction interface may also terminate at these same latitudes (Fig. 8). Two other boundaries suggested by

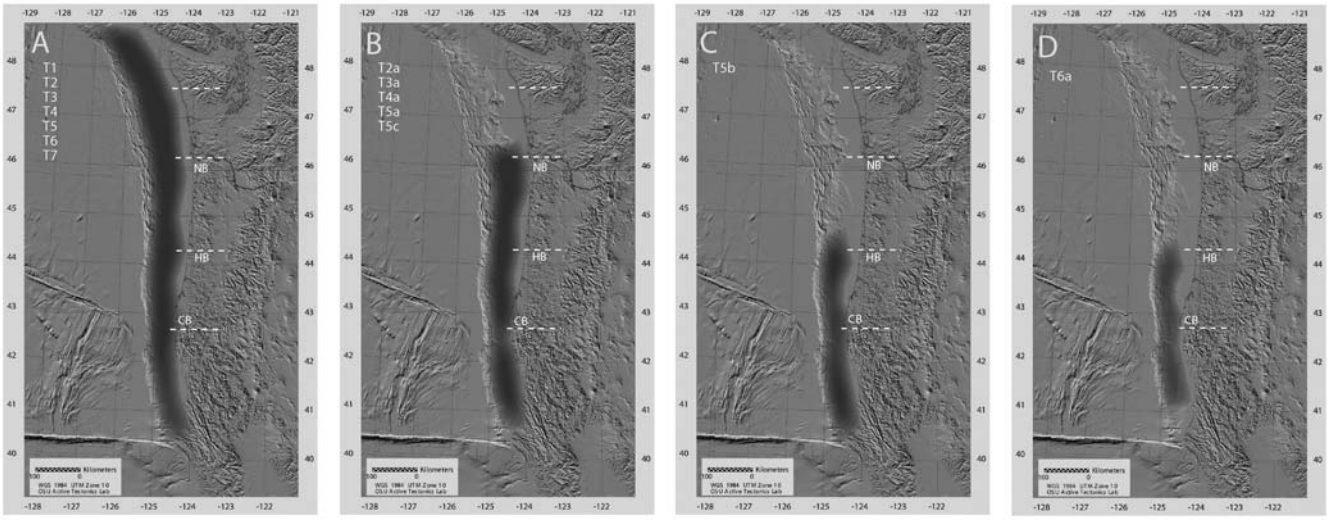

Figure 8. Late Holocene rupture lengths of Cascadia great earthquakes for the ~3000-yr period discussed in this article. Four panels showing preliminary rupture modes identified using turbidite correlation. (a) Full rupture, represented at all sites by seven events. (b) Mid-southern rupture, represented at all sites as far south as 40.7° N by five events. (c) Southern rupture from central Oregon southward to at least 41° N, represented by one event. (d) Southern Oregon/northern California events, represented by one event. Ⓔ Slightly varying southern limits from turbidite data shown the same here are given in Table 4 of the electronic edition of *BSSA*. Rupture terminations appear to occur at three forearc structural uplifts: Nehalem Bank (NB), Heceta Bank (HB), and Coquille Bank (CB). Approximate updip and downdip limits from Clarke and Carver (1992), Goldfinger *et al.* (1992, 1996), Oleskevich *et al.* (1999), and Goldfinger (2007). Paleoseismic segmentation shown corresponds well to the latitudinal boundaries of episodic tremor and slip (ETS) events proposed for the downdip subduction interface (Brudzinski *et al.*, 2007). These boundaries are shown by white dashed lines. A northern segment proposed from ETS data does not appear to have a paleoseismic equivalent.

ETS recurrence periods for Washington seem not to correlate with paleoseismic evidence presented here.

NSAF Event Correlation

We have added color data analysis to the correlation of events along the length of the NSAF margin presented in Goldfinger *et al.* (2007). Color analysis is of greater resolution than the magnetic or density traces, with scan lines of 1 mm; however, these data are subject to surface irregularities on the surface of the split core. Nevertheless, for many intervals, the detailed color traces offer additional correlation ties and strengthen the stratigraphic framework. The correlation is made within a ^{14}C-age framework, with some vertical stretching of cores required due to varying sedimentation rates.

Goldfinger *et al.* (2007) show a regional correlation of NSAF turbidite stratigraphy spanning the Holocene. Here we focus on the upper ~2800 yr of record, making use of high-resolution magnetic susceptibility data (3-mm spacing, point sensor) and color reflectivity data. Our Noyo Canyon cores, 49PC and companion Kasten core 54KC, are particularly important because unlike all the other channel systems, Noyo Canyon is actually cut and offset by the NSAF. Most likely for this reason, the turbidite record there is expanded in thickness, making investigation of the details of each event much clearer in those cores. Cores to the south have much reduced sedimentation rates, even though they are closer to the Russian River source, the largest river along the north coast section of the NSAF. Possible reasons for this are discussed in Goldfinger *et al.* (2007). By comparison to the robust Noyo record, most of the events along the NSAF in other channels are subdued, and indeed the upper 10 events shown in these figures are very fine silt turbidites not visible to the naked eye. Their unique signatures in the physical property data, however, allow good correlation between sites. Ⓔ We have collapsed a much larger set of core records onto the representative correlation diagrams shown in Figure 3 in the electronic edition of *BSSA*. A key stratigraphic datum in this correlation is T11, which is a robust event correlated and visible as a sandy turbidite in all cores, dated at 2574 (2397–2681) yr B.P. in Noyo Channel, and 2256 (2080–2401) yr B.P. in Gualala Channel. We suspected that the original ^{14}C age for this event (~2600 yr B.P.) was too old (possible basal erosion) and have used constraints from hemipelagic sedimentation rates surrounding this interval to estimate the ~2100-yr B.P. age in Ⓔ Figure 3 of the electronic edition of *BSSA* (Goldfinger *et al.*, 2007).

As in Cascadia, correlation of individual events based on the grain size distribution represented by the magnetic and density data are possible both along strike and down channel. Robust event signatures that can be recognized both within single channels, between multiple channel systems, and above and below confluences support the inference that they in fact represent the same source events, independent of other methods. We observe that the correlated events retain their essential character, typically made up of a stack of coarse pulses, for considerable distances along the margin. The signatures are observed to evolve downstream where coarse pulses merge with distance from the margin. The event signatures also evolve to some extent along strike in some cases, although in other cases stratigraphic sections at opposite ends of the fault system match as well as close neighbors. These properties can be observed through close inspection of Figures 3–6, Ⓔ Figure 3 of the electronic edition of *BSSA*, and Goldfinger *et al.* (2007).

NSAF Confluences and Mineralogy. At the site of core 24GC, below several confluences of Viscaino, Noyo, and Gualala Channels (confluences shown in Fig. 2), we find that multiple coarse pulses reveal the heavy mineral assemblage from individual canyon sources, stacked vertically in order of arrival at the core site. The turbidites at this site also have no hemipelagic sediment between the sand pulses, indicating little time passage between the deposition of the pulses (see the timing discussion later in this article). The alternative, removal by erosion, is possible, but would have to occur at each turbidite base at every correlative site. Further downstream, we observe bimodal heavy mineral coarse fractions, with mineralogical peaks representing the separate provenance components (Goldfinger, Nelson, and Johnson, 2004). We observe no significant changes in the stratigraphy between upstream and downstream sites, despite input from multiple sources at the confluences. Further downstream at the site of core 31PC, we find that individual turbidites have the same stacking of coarse pulses, but the provenance input is less distinct, suggesting further mixing downstream. This can also be observed directly in the downstream evolution of each turbidite. Goldfinger *et al.* (2007, fig. 3) show a typical example of a two-pulse turbidite as the two pulses begin to merge along the 74-km distance between the proximal and distal cores. This evolution is expected as the turbidity current wanes and originally separated internal structures become less distinct downstream. Goldfinger *et al.* (2007) show stratigraphic correlation details for a series of cores upstream, near, and downstream of the confluences of Viscaino, Noyo, Gualala, Albion, and Cordell Channels. The data span the time period from ~3500 to ~10, 000 yr B.P. because the upper section is poorly preserved in some of the downstream cores. The downstream cores have, as yet, only a few dated turbidites, in part due to the low foraminifer abundance at water depths in excess of 3500 m at these sites. The section ages are bounded by several late Pleistocene ages, and the age of 4676 (4525–4810) yr B.P. for T18 in core 26PC, which we use to constrain the upper part of the correlation.

While additional ^{14}C ages are still needed, we can test for synchroneity by carefully matching events between upstream cores at Noyo and Gualala Channels and correlative events in the downstream cores in this time range. We matched the stratigraphy and checked for presence/absence of hemipelagic sediment between events (or an erosive event

that removed it), as well as the multiple cues used in physical property based stratigraphic correlation. We observe that upstream (49PC) and downstream cores (e.g., 25GC) both contain 22 events in this time range. Differences between the two are minor, and appear mostly attributable to local basal erosion. Included in the confluence analysis of Goldfinger *et al.* (2007) is a correlation with core 31PC, which is actually below a total of four confluences, with input from a total of six channels, while cores 24GC, 25GC, and 26PC each sample three channels. The good correlation between these cores suggests that input mixing at each confluence has little effect on the stratigraphy of the turbidites, even though the number of sources increases at each confluence. We infer that synchronous triggering is the only viable explanation for this, and are unable to suggest an alternative. Nonsynchronous triggering should produce an amalgamated record that increases in complexity below each confluence, with only partial correlations, if any, for the synchronous events. The mixing and stacking of the provenance components further suggests synchronous arrival at the confluence.

We observe that while the overall stratigraphy of the turbidite sequence is maintained through confluences, the internal complexity and stratigraphic thickness of some events actually increases for distal cores, just the opposite behavior expected for distal sites where thinning and homogenization of turbidites would be expected. We attribute this to the reinvigoration and addition of new material injected at each confluence, and potentially to the slight mistiming of coarse pulses expected due to variable travel times for channel tributaries.

From these results, we infer that the events and sites included in this analysis pass a strict test of synchroneity, and are most likely of earthquake origin. Further analysis of the remaining confluence sites is in progress. A similar use of mineralogic provenance to fingerprint source channels and test for earthquake origin has been used in the Sea of Japan by Shiki *et al.* (2000).

NSAF Radiocarbon Time Series and Comparison to Onshore Paleoseismic Sites. In terms of event ages and their distribution in time, the youngest 15 NSAF events have a mean repeat time of ~200 yr, with a standard deviation of 60 yr. Using peak probability density function (PDF) values for event ages, the minimum interval value is ~95 yr between T7a and T7 and T12a and T12, and the maximum value is ~270 yr between T5 and T6 and T10–T11 (we refer to the third event as T3–4 because it is a doublet that may yet prove to be two events). We find these values reasonably consistent with previous paleoseismic data onshore. The ages shown in Figure 9 include 11 ages reported by Zhang *et al.* (2006) from the Vedanta Marsh site, two ages reported by Knudsen *et al.* (2002) at Bodega Bay and Bolinas Lagoon, and five ages reported by Kelson *et al.* (2006) from sites at Fort Ross. The PDF curves for ages in Figure 9 are color shaded to represent the time interval constraint from the hemipelagic sediment between events. The center (dark) part of the PDF represents the unconstrained part of the PDF, and the two outward lightening shades represent 100% and 75% of the full hemipelagic constraint as used in OxCal. These constraints cannot strictly trim the distributions because they are not completely independent constraints (the sedimentation rates depend on the ^{14}C ages); however, the position of these constraints is part of the OxCal output when the ages and hemipelagic constraints are input in stratigraphic order.

These results indicate that the penultimate event probably occurred between A.D. 1700–1750 north of San Francisco. The mean age for this event from all sources is indistinguishable from A.D. 1700. The age correspondence between NSAF land and marine data is good for the last ~2300 yr when comparing Noyo Canyon marine ages to Vedanta Bolinas and Fort Ross land ages. For a given time interval when individual land records overlap with the marine record, we see approximately the same total number of events (± 1) onshore and offshore, suggesting either a coincidence or that land and marine sites are recording the same events. Further support for a linkage between the turbidite series presented here and onshore earthquakes, is the good correspondence between land and turbidite recurrence intervals, which are 200 and 240 yr for marine and land ages, respectively. Individually, most ages except Noyo T3–4 (a doublet) and T7a have significant overlap of age ranges (Fig. 9). Tom Fumal (T. Fumal, personal comm., 2007) reports that an additional event has been found in a new trench at Vedanta, which may correspond to the second event in our T3–4 couplet. Our event T3–4 was not reported at Fort Ross, and our event T9 was apparently not observed at Vedanta. Our current stratigraphic correlation and age series, taken together, suggest that the previous 11 events may be correlated from Noyo Canyon to at least to the latitude of Vedanta, just north of San Francisco. Our initial along-strike correlations imply rupture lengths for many (or most) events of > 250 km. Other events may well have occurred, but without being recorded (or yet discovered) either offshore or onshore.

Temporal Association of Southern Cascadia and NSAF Earthquake Series

Cascadia-NSAF Temporal Comparison

The average recurrence interval for the southern Cascadia margin in the last ~3000 yr (ignoring the slightly different southern rupture limits) is 223 yr (3154 (average age of T7) $- 250)/13 = 223$ yr). The similarity between the mean NSAF recurrence time and the southern Cascadia recurrence (~200 offshore, 230 onshore versus ~223 yr, respectively) and the relatively close correspondence between the A.D. 1700 Cascadia event and the penultimate NSAF event, at A.D. ~ 1700–1760, prompted us to examine both the temporal connection between the two fault systems and the potential stress interactions between them. In Figure 9, we plot the NSAF time series over the past ~3000 yr with Cascadia events shown using both peak probability and PDF functions for offshore turbidite ages and onshore paleoseismic data.

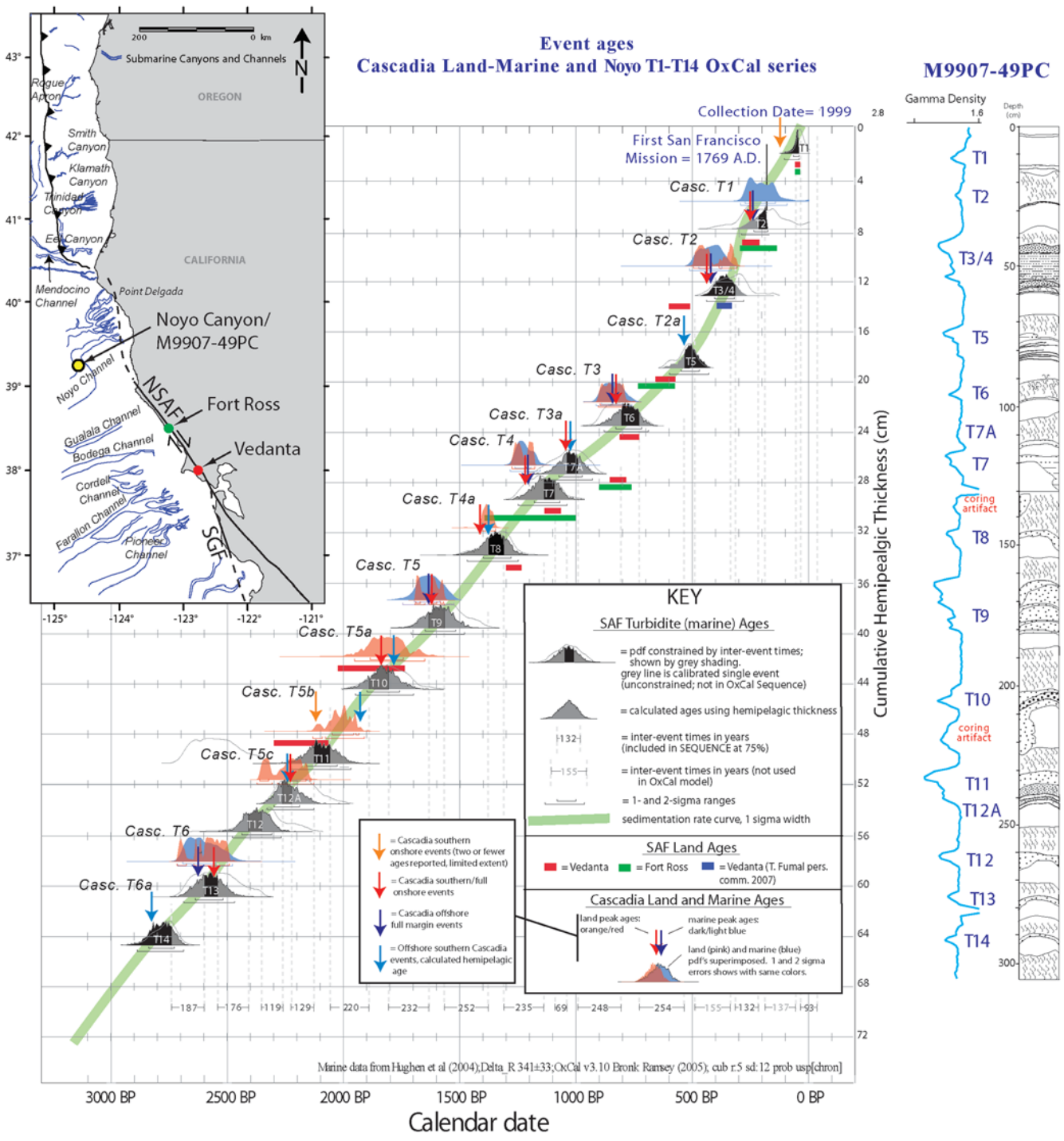

Figure 9. OxCal age model for the youngest 15 events in the NSAF offshore system, onshore NSAF ages, and comparison to Cascadia event ages. Cascadia OxCal PDFs are shown in blue. Land ages from OxCal combines are shown in red. Cascadia mean event ages are also shown with blue arrows for well-dated turbidite events, light blue arrows for hemipelagic age estimates, and red arrows for onshore paleoseismic events. See text for discussion and tables for data used and criteria, and discussion of temporal relationships. Interevent times based on hemipelagic sediment thickness (represented by gray segments of NSAF PDFs) were used to constrain original NSAF ^{14}C calendar-age distributions (gray traces) using the SEQUENCE option in OxCal. Interevent times were estimated by converting hemipelagic sediment thickness between each pair of events to time using the sedimentation rate. Events dated more than once were combined in OxCal prior to calibration if results were in agreement; if not in agreement, the younger radiocarbon age was used in the final model. Five ages are calculated from sedimentation rates where not enough forams were present for ^{14}C dating. The resulting probability distributions (filled gray) are mostly in good agreement with land ages from Fort Ross except for T3–4 and T7a (green lines; Kelson *et al.*, 2006), Vedanta (red lines; Zhang *et al.*, 2006), Bolinas Lagoon and Bodega Bay (purple lines; Knudsen *et al.*, 2002), and Point Arena (light blue lines; Prentice *et al.*, 2000). Additional Vedanta event is also shown (T. Fumal, personal comm., 2007). See inset for geographic locations. The vertical scale is cumulative hemipelagic sediment thickness. Ⓔ See the electronic edition of *BSSA* for OxCal input data and further detail of sedimentation-rate curve.

For Cascadia marine events that have multiple ages for the same event, we first exclude outliers, then combine the well-correlated ages using the Bayesian method in OxCal. The statistical merging of the PDFs for these events yields a narrower PDF for a single event dated independently with multiple samples. For land ages, we use the combined land-marine dataset to determine the best ages to use for this study based on their reported error ranges, the fit of the reported age to the larger dataset, and the fit of the age within the data reported by the original authors for land data. In most cases we have adopted the rationale used by the original authors to report their preferred ages for each event. In some cases we have further culled multiple ages to remove outliers. Ⓔ The ages selected for use in this study and original references are given in Table 1 of the electronic edition of *BSSA*. Since the full original data were not always published, we have obtained the lab data from original authors and recalibrated the ages used in OxCal, yielding a more consistent representation of single and combined ages. In two cases, there are land ages reported for which there are only one or two reported ages and no observed turbidite evidence. These are shown with separate symbology in Figure 9. These could either be spurious bad ages in the land record, or a real event of limited spatial extend not observed in the marine record.

In addition to the close correspondence between the Cascadia A.D. 1700 earthquake, and the penultimate NSAF event ~1700–1760 and recurrence intervals noted previously, we also see an apparent coincidence of Cascadia events and NSAF events occurring at approximately the same time for 12 and possibly 14 of 15 NSAF earthquakes (Fig. 9; Goldfinger *et al.*, 2007). During the 0–3000-yr period, the combined onshore/offshore paleoseismic record for Cascadia includes 12 events, and 2 possible additional events. The thirteenth event is recorded by significant subsidence in Eel River Basin in the early 1800s, though it is not observed elsewhere and not known in the offshore paleoseismic record, which is only poorly known at Eel Channel at present (Carver and Plafker, 1999; Carver, 2000). The fourteenth event is one that includes three reported land ages (two of high quality) in the range 2100–2255 yr B.P. in central and southern Oregon, and a small turbidite event. This event, T5c, is undated offshore, but we include a calculated age based on the hemipelagic sediment accumulated above well-dated T6 (Fig. 6).

To a first order, the recurrence intervals for southern NSAF and Cascadia (200 versus 220) are quite similar, and clearly distinct from northern Cascadia (496–526 yr; Goldfinger, Morey, Erhardt, *et al.*, 2006; C. Goldfinger *et al.*, unpublished manuscript, 2007). If we include the uncertain 1800s event described previously, the average repeat time for southern Cascadia would be 212 yr over the last 3000 yr. For the 15 NSAF events, we observe that with the exception of NSAF event T12 (and the weaker associations of T12 and T1), the remaining NSAF earthquakes each have a corresponding Cascadia event in temporal proximity. The relationship can be seen graphically in Figure 9. The question arises then: Is this similarity in time series coincidental? While considerable uncertainty exists in comparing ^{14}C ages, the marine record brings significant advantages in terms of constraining event ages. First, we have focused on several key cores from both systems in which the majority of the events are dated, and thus are constrained to be in stratigraphic order (also true for land sites). The remaining event ages come from cores that have been stratigraphically correlated. This constraint is significant and reduces the possibility of miscorrelation that plagues onshore paleoseismology, though of course is subject to errors of interpretation. In Figure 9 we summarize the two time series and the relationship between them. For all NSAF events, we have used the relaxed hemipelagic constraint (75% of the calculated time interval) in the OxCal calculations. In the figure, we show this graphically by shading the portions of the PDF that fall within these time intervals, and thus are less likely to contain the time of the event. The PDFs themselves reflect the relaxed constraint, but statistically do not terminate abruptly at these boundaries. Full constraints using hemipelagic data for the Cascadia margin are not used in this study, and await completion of the reservoir model discussed in a subsequent section of this article.

We can examine the temporal relationship (if any) between the NSAF and southern Cascadia by several methods: the relationship of mean ages, peak probability ages, and probability distributions. We have calculated the means from the midpoint in the 2-sigma ranges for Cascadia events in several groupings: the mean for offshore correlated events, the mean for onshore events thought to correlate, and the combined means. These, along with the probability peak ages are given in Tables 1 and 2, which include comparisons to the NSAF data. Ⓔ The ages used and sources are given in Tables 1–3 in the electronic edition of *BSSA*. We use ages calculated from marine sedimentation rates for only a few cases where the event was not datable or the number of ^{14}C ages for a given event was low. Several of the smaller local southern-Cascadia-inferred events could not be dated with ^{14}C, and for these events we calculate the age based on well-constrained bracketing events above and below, using hemipelagic thickness and the local sedimentation rate.

Comparing raw means for 12 events for which we can make a comparison, the Cascadia turbidite events differ from NSAF events by an average 36 yr (S.D. 28 yr), with 12 means preceding NSAF and three virtually identical. The time interval by which NSAF events preceded Cascadia is 150 yr, larger by a factor of ~4 (Table 1; Ⓔ Fig. 4 in the electronic edition of *BSSA*). For events interpreted to be the same events onshore (excepting Cascadia T2a and T6a, which may not be observed), 9 of 12 Cascadia peak ages precede NSAF events, with three ages nearly identical, yielding an average delta of 37 yr (S.D. 42 yr) The alternate hypothesis of NSAF precedence yields a mean delta of 202 yr, greater by a factor of ~5 (Table 2). Comparing peak and midpoint PDF ages from marine-correlated ages combined with OxCal where possible yields a slight narrowing of the delta to 37 and 26 yr, respectively, or 159–170 yr for NSAF preceding Cascadia, larger by

Table 1

Comparison of Marine NSAF Ages with Marine OxCal Combined Ages and Peak Single Ages from Cascadia Marine Data

				Marine OxCal Combine		Marine OxCal Peaks		Marine OxCal Mid		Marine Peak Means	
NSAF Event No.	NSAF Mean Peak Age	Cascadia Event No.	Mean Peak Turbidite Age	Peak	Mid	Predate Delta	Postdate Delta	Predate Delta	Postdate Delta	Predate Delta	Postdate Delta
1	44										
2	230	1	246	250	205	−20.0	115	25.0	160	−15.5	119
3–4	365	2	425	410	388	−45.0	100	−23.0	122	−59.6	85
5	510	2a	512							−2.4	263
6	775	3	800	815	830	−40.0	215	−55.0	200	−25.4	230
7a	1030	3a	1030*							−0.1	105
7	1135	4	1214	1240	1232	−105.0	100	−97.0	108	−79.4	126
8	1340	4a	1384							−43.9	206
9	1590	5	1682	1535	1557	55.0	295	33.0	273	−91.9	148
10	1830	5a	1856*							−25.5	239
11	2095	5b	?								
12a	2250	5c	2277*							−27.0	103
12	2380										
13	2570	6	2601	2640	2610	−70.0	130	−40.0	160	−30.6	169
14	2770	6a	2812							−42.5	
		7	3130	3210	3210						
					Mean delta	−37.5	159.2	−26.2	170.5	−37.0	149
					S.D.	53.9	79.2	49.3	59.8	28.3	62

*Calculated age. Delta is defined as the time difference (years) between NSAF and Cascadia earthquakes.

Table 2

Comparison of Cascadia Land Ages, Combined Cascadia Land–Marine and Cascadia OxCal Combines with NSAF Marine Event Ages

		Land Mean		OxCal Peak Land							With Prototype Reservoir Model Peak Means	
Onshore Mean Cascadia Age	Cascadia Event No.	Predate Delta	Postdate Delta	Age	Predate Delta	Postdate Delta	Combined Land–Marine Mean	Predate Delta	Postdate Delta	With Prototype Reservoir Model Turbidite Age	Predate Delta	Postdate Delta
120		−76.0	110									
250	1	−20.0	115				247.8	−17.8	117.2	246	−15.5	119
448	2	−83.0	62	335	30.0	175.0	436.3	−71.3	73.7	425	−59.6	85
No record?	2a									530	−20.3	245
846	3	−70.8	184	690	85.0	340.0	823.1	−48.1	206.9	787	−11.9	243
1050	3a	−20.0	85				1040.1	−10.1	94.9	1030	−0.1	105
1217	4	−81.7	123	1200	−65.0	140.0	1215.5	−80.5	124.5	1198	−63.1	142
1428	4a	−87.5	163	1385	−45.0	205.0	1405.7	−65.7	184.3	1384	−43.9	206
1622	5	−31.7	208	1685	−95.0	145.0	1651.8	−61.8	178.2	1585	5.1	245
1808	5a	22.0	287	1820	10.0	275.0	1831.8	−1.8	263.2	1856	−25.5	239
2120	5b	−25.0	130	2000	95.0	250.0	2120.0	−25.0	130.0	1842		
2228	5c	22.5	343	2220	30.0		2252.2	−2.2		2277	−27.0	
2560	6	10.0	210	2580	−10.0	190.0	2580.3	−10.3	189.7	2501	69.4	269
No record?	6a									2712	57.5	
3021.25	7									3050		
	Mean delta	−36.8	202	Mean delta	4.4	215.0	Mean delta	−39.4	156.3	0	−11.2	190.0
	S.D.	41.9	83	S.D.	64.6	69.0	S.D.	30.0	60.6		40.7	69.4

a factor > 4 (Table 1, 2-sigma ranges given in Table 3). Land OxCal peaks differ from the NSAF by an average of 4 yr (but S.D. is large at 65) and 215 yr for predate and postdate, respectively. Combined land/marine Cascadia mean ages differ from NSAF events by an average of 39 yr, with 11 preceding and 5 events nearly identical in age (Table 2). The mean postevent delta is 156 yr, larger by a factor of ~4. The preceding deltas calculated by five methods are all statistically indistinguishable from one another considering the associated error budgets, as are the postdate deltas.

Comparison of the PDFs for Cascadia and NSAF events in Figure 9 shows that the PDFs of most events from both regions have overlap at the 95% level; however, the time between events represented by hemipelagic sediment, and shown in the figure, reduces considerably the probability that earthquakes occurred in the low probability portions of the PDF. Regionally, most events for each system are also precluded from overlap by virtue of being in stratigraphic order in a single core, or well correlated between cores for the marine data. The detailed comparison of ^{14}C ages is of course fraught with multiple uncertainties, and should be considered with caution.

One additional uncertainty is the reservoir correction applied to marine ages to obtain calendar ages (Stuiver and Braziunas, 1993). This value, representing the age of the seawater populated by microfossils we use to date the turbidites, is a published spatially varying value specific to west-coast sites. The published value is derived usually from paired shell/wood dates that establish the age of the water in which some shelled animals lived with stratigraphically correlated terrestrial material. The published values are almost exclusively from the twentieth century, though it is known that these values change through time (i.e., Kovanen and Easterbrook, 2002). We have observed probable time and space variant mismatches between land and marine ages for the same earthquake events, for earlier periods of time, and have attempted to map the variability using the numerous ages from the land and marine earthquake record as part of an ongoing separate investigation. This mapping is included in Ⓔ Table 2 of the electronic edition of *BSSA* and shown graphically in Figure 7. If we apply this prototype reservoir model to our marine ages, we find that in addition to tighter groupings of land-marine ages, which would be expected, the mean delta between the NSAF and preceding Cascadia earthquakes is reduced to 11 yr. For Cascadia, following the NSAF, the delta is 190 yr, larger by a factor of > 17. Application of this prototype reservoir age mapping is not included in Figure 9; however, its application appears promising and is included in Table 2 for comparison.

The age series in total suggest a temporal relationship between Cascadia and NSAF events that does not appear to be random and strongly favors Cascadia earthquakes preceding the NSAF The alternate relationship that Cascadia events consistently postdate NSAF events is possible as well, though the average time separation would be greater by a factor of 4–6. We also note that the Cascadia ages for offshore events may change somewhat as a result of better definition of the marine reservoir correction in the future, and this may help close the gap for some time and latitude ranges for which the modern correction appears to be inadequate.

Dynamic Links between the Cascadia Megathrust and the NSAF

Coseismic and Postseismic Deformation from Cascadia Earthquakes

In order to quantify the influence of Cascadia earthquakes on the NSAF, we model the coseismic and postseismic deformation from the Cascadia earthquake. First we verify the geometry of the NSAF system, which has only

Table 3
Summary of Error Ranges for OxCal Marine-Combined Data

NSAF Event Number	NSAF 2-sigma Ranges	CASC OxCal 2-sigma Ranges	Cascadia Event Number	Turbidite Age	Cascadia Marine 2-sigma Ranges
T1	39.5–104.5				
T2	169.5–289.5	101–287	1	246	155.3–328.3
T3/4	279.5–439.5	298–460	2	425	325.5–503.1
T5	429.5–599.5		2a	512	
T6	689.5–879.5	742–907	3	800	684.3–916.3
T7A	929.5–1119.5		3a	1030	
T7	1039.5–1249.5	1162–1287	4	1214	1113.4–1328.4
T8	1249.5–1469.5		4a	1384	
T9	1479.5–1709.5	1527–1731	5	1682	1542.8–1783
T10	1699.5–1949.5		5a	1856	
T11	1969.5–2229.5		5b	?	
T12A	2129.5–2329.5		5c	2277	
T12	2269.5–2479.5				
T13	2469.5–2689.5	2480–2706	6	2601	2497.5–2756.7
T14	2689.5–2889.5		6a	2812	
		3090–3321	7	3130	3027.2–3263.4

been poorly mapped previously. Offshore, the NSAF traverses the continental shelf between Point Arena and Point Delgada and was mapped using early seismic reflection profiles (Curray and Nason, 1967). In 2004, we collected multibeam bathymetric data and several 3.5-kHz profiles across the offshore NSAF. We used these data and a newly released dataset of migrated industry multichannel reflection profiles to verify that the NSAF indeed traverses the shelf and comes ashore again at Point Delgada (Fig. 10) and verify the original mapping of Curray and Nason. We also observe some additional compressional deformation, particularly within the northeast part of the Viscaino block, but are unable to evaluate this deformation in terms of recency and rates, and thus we do not consider it in the subsequent modeling.

We model the elastic coseismic deformation, deformation from deep afterslip, and 60 yr of postseismic deformation resulting from viscoelastic relaxation of elastic stress changes due to the earthquake in the mantle. We initially assume that the entire subduction zone slipped in a megathrust event such as the A.D. 1700 earthquake (Satake *et al.*, 1996; Goldfinger *et al.*, 2003a; Satake *et al.*, 2003) and also model a smaller southern-margin earthquake.

The first-order slip model involves 14 m of slip on each of the 16 planes spanning the 1050-km-long megathrust rupture and 7 m of slip on the 8 deep afterslip planes. The elastic coseismic and postseismic deformation is calculated in a layered spherical geometry using the method of Pollitz (1996). The geometry of the megathrust rupture is based on the plate-interface model of Flueck *et al.* (1997), and the elastic structure of the Earth is based on the seismically determined global Earth model, Preliminary Reference Earth Model (PREM; Dziewonski and Anderson, 1981). The modeled earthquake has a magnitude of M_w 9.1 based on the fault geometry, slip values and Earth model. Viscoelastic deformation is calculated on a spherical Earth using the method of Pollitz (1992). We use the preferred spherically layered Earth model presented by Pollitz *et al.* (2006) for a study of postseismic deformation following the 2004 and 2005 Sumatra megathrust events, which employs a biviscous (Burgers body) viscoelastic rheology in the asthenosphere (Pollitz *et al.*, 2006). In this model, the asthenosphere has an initial short-term viscosity of 5×10^{17} Pa s that dominates the deformation during the first few years and a long-term viscosity of 1×10^{19} Pa. This model matches both the spatial pattern and temporal evolution of the first year of postseismic Global Positioning System (GPS) measurements in Southeast Asia. The modeled postseismic surface velocities after several decades of transient deformation are also of similar magnitude as those currently measured along the rupture zones of the great 1960 Chile (Hu *et al.*, 2004) and 1964 Alaska (Zweck *et al.*, 2002) earthquakes.

Figure 11a,b,c shows the far-reaching surface displacement fields (only displacements < 0.3 m are shown) from the coseismic and postseismic deformation models. The horizontal coseismic displacements near the updip end of the rupture approximate the 14 m of modeled slip and decrease to about 2 cm in the San Francisco Bay Area (Fig. 11a; Ⓔ Fig. 5 in the electronic edition of *BSSA*). Coseismic displacements exceeding 0.1 m extend for up to 500 km to the east and west of the rupture. The vertical displacements from our coseismic model are to a first-order compatible with the subsidence observed and estimated from coastal marsh studies for the 1700 earthquake (compiled in Leonard *et al.*, 2004). Detailed matching of subsidence data is made problematic however by the complexities of the onshore accretionary wedge in southern Cascadia, the unknown slip distribution of the 1700 earthquake, the multiple subsidence methodologies used, and the weak constraints imposed by these methodologies. The horizontal surface displacements resulting from deep afterslip peak at about 2.5 m and are between 2–3 cm in the Bay Area (Fig. 11c; Ⓔ Fig. 6 in the electronic edition of *BSSA*). The cumulative motions from mantle relaxation in the first 60 yr of postseismic relaxation exceed 0.1 m to distances greater than 1000 km. The horizontal viscoelastic displacements at the surface peak at about 1.65 m and are between 0.15–0.25 m in the Bay Area (Fig. 11b; Ⓔ Fig. 7 in the electronic edition of *BSSA*). However, except for the segment offshore from Point Delgada, the NSAF is located in a low-strain lobe for both the coseismic and postseismic deformation.

Stress Changes from Cascadia Earthquakes along the NSAF

We evaluate the stress changes along the NSAF associated with coseismic and postseismic deformation from Cascadia megathrust events in order to test the possibility that Cascadia earthquakes triggered subsequent NSAF events. We model the Coulomb failure stress (CFS), which takes into consideration both shear- and normal-stress changes across the NSAF. Previous studies have shown that CFS increases of 1–3 bars are generally sufficient to trigger seismicity (e.g., Stein and Lisowski, 1983; Toda *et al.*, 1998; Rydelek and Sacks, 1999; Freed, 2005). We use a CFS function given by $\mathrm{CFS} = \Delta\tau + \mu'\Delta\sigma_n$, which defines CFS as a sum of the change in shear stress τ and the change in normal-stress σ_n, multiplied by an effective coefficient of friction μ. Positive CFS enhances loading on the right-lateral NSAF. CFS is modeled on 48 NSAF receiver-fault segments at 10 km depth, based on the geometry of the 1906 earthquake rupture (Thatcher *et al.*, 1997), assuming $\mu' = 0.4$. CFS values are also computed for a ~100-km-wide zone along the NSAF, assuming the same receiver-fault geometry.

Deformation and stress changes from megathrust earthquakes are large and far reaching (e.g., Banerjee *et al.*, 2005; Nalbant *et al.*, 2005). Significant postseismic deformation transients due to viscous relaxation in the mantle further expand the reach of fault interactions and are likely to persist for many decades (e.g., Pollitz *et al.*, 1998, 2006). The magnitude of CFS change on a nearby fault depends on the relative position, its orientation, and distance to the earthquake source. Thus, stress changes along the NSAF due to a Cas-

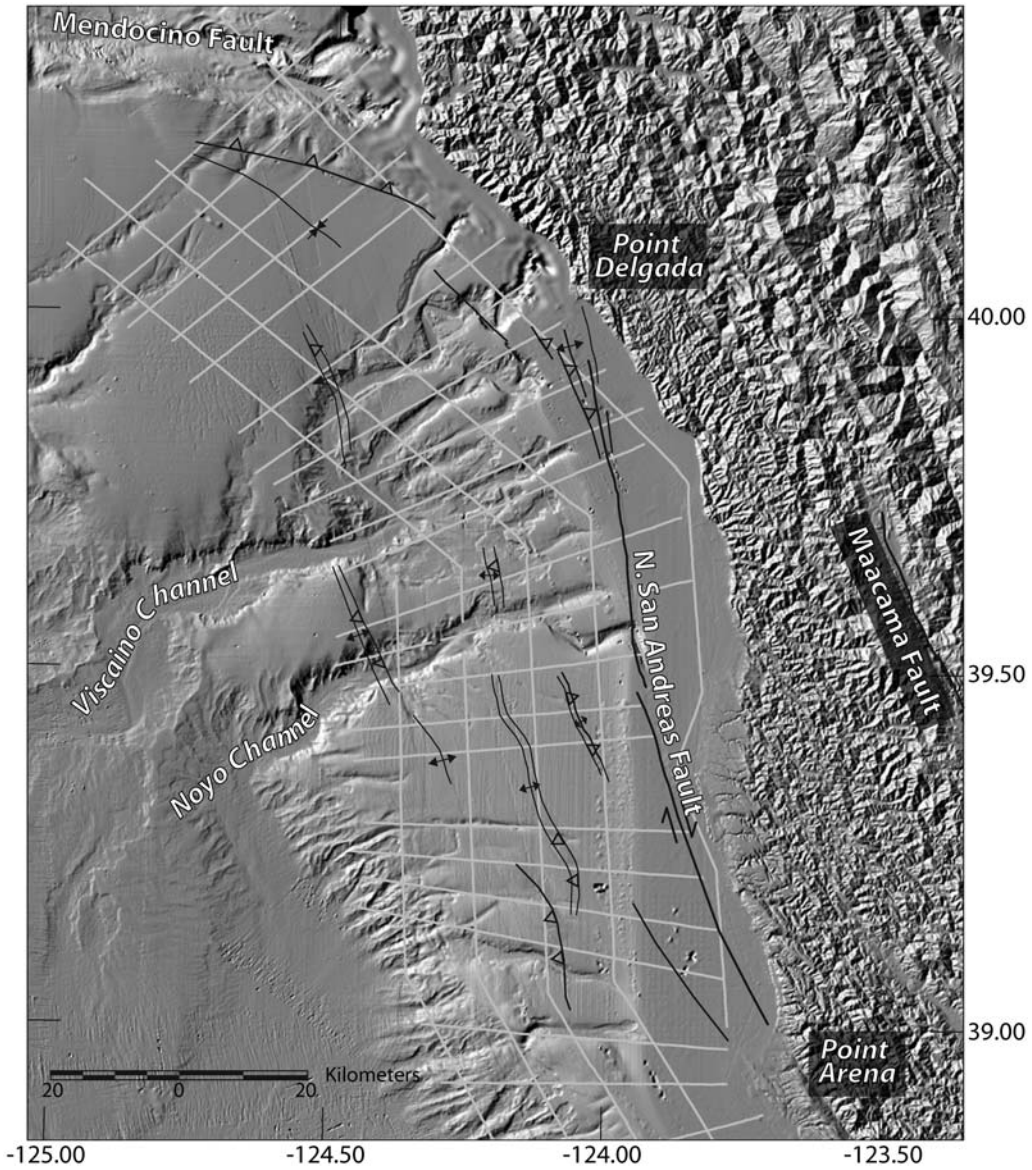

Figure 10. Shaded relief image and structure map of the offshore NSAF region. NSAF trace was mapped using multibeam bathymetry from Point Arena to Point Delgada, and recently released industry multichannel seismic reflection profiles (tracklines shown in gray). Remapping main offshore trace shows original mapping by Curray and Nason (1967) to be correct, and main trace comes ashore again at Point Delgada. NSAF offsets and captures the head of Noyo Canyon at the N in the San Andreas fault. Additional details of the fault trace show modest stepovers and additional deformation of the northeast Viscaino block.

cadia megathrust rupture and subsequent relaxation vary significantly along the fault due to both changes in distance and strike of the fault, ranging from N55W to N1W. Overall, we find that coseismic CFS changes are large and likely to enhance subsequent rupture only on the northernmost segment of the NSAF (Fig. 12a). CFS changes along the remainder of the fault are modest, as the NSAF lies in a nodal lobe of coseismic deformation. Postseismic viscous relaxation appears to reduce CFS along much of the NSAF and can therefore not be considered as a significant triggering mechanism in this case. Future work will evaluate if consideration of three-dimensional heterogeneity of Earth rheology significantly changes this conclusion.

The coseismic deformation increased CFS at 10 km depth by a maximum of about 9 bars in the section of the fault near Point Delgada (Fig. 12a). The CFS resulting from the viscous deformation peaks at about 2.5 bars; however, this peak is in the northernmost region of the fault where there is a large negative coseismic CFS (Fig. 12c). Postseismic afterslip both increases and reduces CFS along the NSAF, but its negative peak reduces the extent of the largest positive coseismic CFS by half (Fig. 12b).

We also compare our uniform-slip full-margin earthquake model with coseismic and postseimic CFS changes resulting from a southern Cascadia earthquake approximating the smaller southern events from the paleoseismic record. We

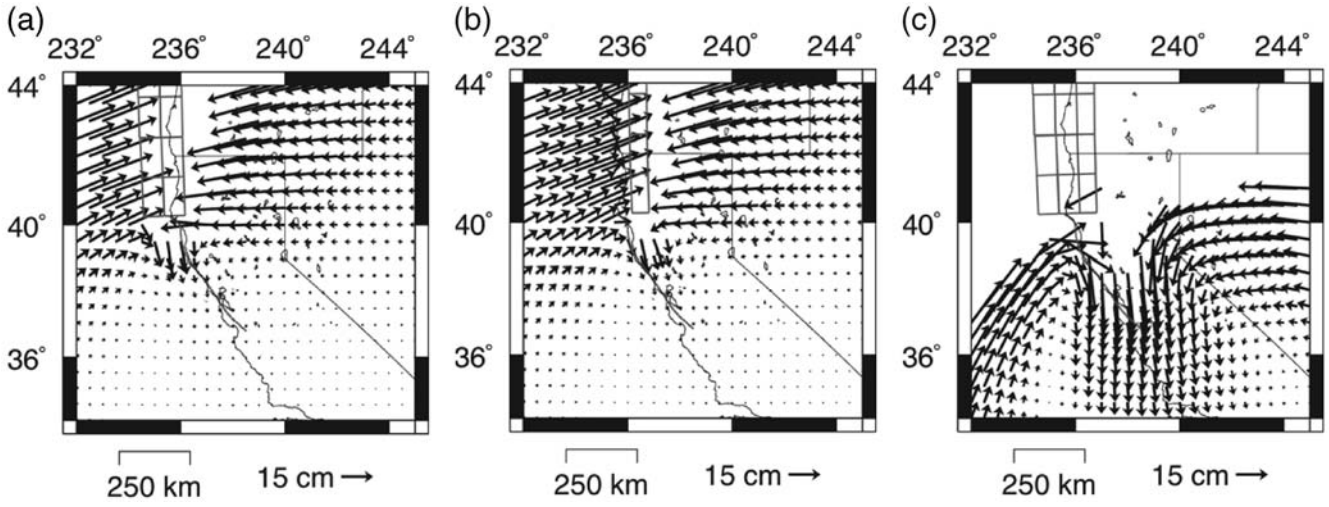

Figure 11. Comparison of the far-field coseismic and postseismic deformation for displacements less than 30 cm at the surface (absent grid points have displacements greater than 30 cm). Ⓔ See the electronic edition of *BSSA* for total displacement fields. (a) Coseismic deformation from Cascade megathrust. (b) Displacement from afterslip on the Cascade megathrust. (c) Cumulative viscoelastic displacement after 60 yr from Cascade megathrust and afterslip.

apply 8 m of slip on the six southernmost Cascade fault planes (380 km strike length) and from a heterogeneous full-margin earthquake that includes less slip on the southern fault planes (Pollitz *et al.*, 2008). Total CFS on the NSAF from both the southern Cascadia earthquake and the heterogeneous full-margin earthquake peaks in the same northern location as from the homogenous full-margin model; however, the CFS peaks are reduced by about a factor of 2. Based on these results, it appears that the most likely nucleation point of a triggered NSAF event, from whichever of the three Cascadia source models, would be near Point Delgada. The coseismic CFS alone would be large enough to trigger an earthquake, while the postseismic contributions from the viscous relaxation and afterslip do not significantly increase the total CFS on the NSAF. This result suggests a directivity to many past NSAF ruptures that is opposite to that of the south–north rupture in 1906, one of the few events that was not preceded by a Cascadia earthquake.

In addition to subduction earthquakes, we also examine the possible contribution from significant triggered slip on the Mendocino transform fault (MTF), the Little Salmon fault (LSF), or the Mad River fault (MRF). A triggered earthquake on the MTF might be expected shortly following a Cascadia earthquake because CFS on the western segment, at 10-km depth, is always positive and peaks at over 40 bars, while CFS changes on the eastern segment fluctuate greatly between about −1000 and 1000 bars. The MRF is not likely to be triggered by the Cascadia subduction zone, as CFS at 10-km depth is always negative with a negative peak of more than −60 bars. A Cascadia megathrust earthquake may trigger an LSF earthquake, as the CFS increases by up to ∼100 bars, and is at least 10 bars for more than 10 km on the offshore part of the thrust fault. Our first-order slip models for the LSF and MTF consist of 2 m of uniform slip based on their characteristic earthquake magnitudes (Clarke and Carver, 1992; McCrory, 1996; Petersen *et al.*, 1996). The combined coseismic and postseismic CFS from 2 m of slip on the LSF peaks at 0.1 bars and would not significantly increase CFS on the NSAF (Fig. 12e). The CFS change on the NSAF from the MTF is highly dependent on the strike and location of the MTF rupture; the 270° striking western segment would only increase CFS on the NSAF by a maximum of 0.4 bars, whereas slip on the 285° striking eastern MTF segment would increase CFS on the offshore NSAF by as much as 30 bars (Fig. 12e). However, the CFS increase from the eastern MTF is located in the northernmost section of the NSAF, where there is a comparably larger decrease in CFS resulting from the combined coseismic and postseismic deformation from the Cascadia earthquake. Therefore, although the eastern MTF on its own could significantly increase CFS on the immediately adjoining, northernmost portion of the NSAF, it would not significantly extend the region of positive CFS when combined with the Cascadia megathrust earthquake.

We also tested the reverse triggering scenario and modeled CFS on the Cascadia receiver planes from an NSAF-type earthquake using a distributed slip model for the 1906 earthquake (Thatcher *et al.*, 1997). The maximum positive coseismic CFS on the southern tip of the margin is about 20 bars at depths between 12–16 km (Fig. 12f). At these depths, CFS increases of at least 1 bar extend north for about 30–40 km. The CFS resulting from viscoelastic relaxation is mostly negative on the southern Cascade receiver planes. This may be sufficient to trigger an earthquake on southern Cascadia or on the smaller upper plate thrust faults, such as the MRF and the LSF, although the 1906 event failed to do so. The paleoseismic record, however, strongly favors the former case, with Cascadia events preceding the NSAF by ∼50 yr, whereas

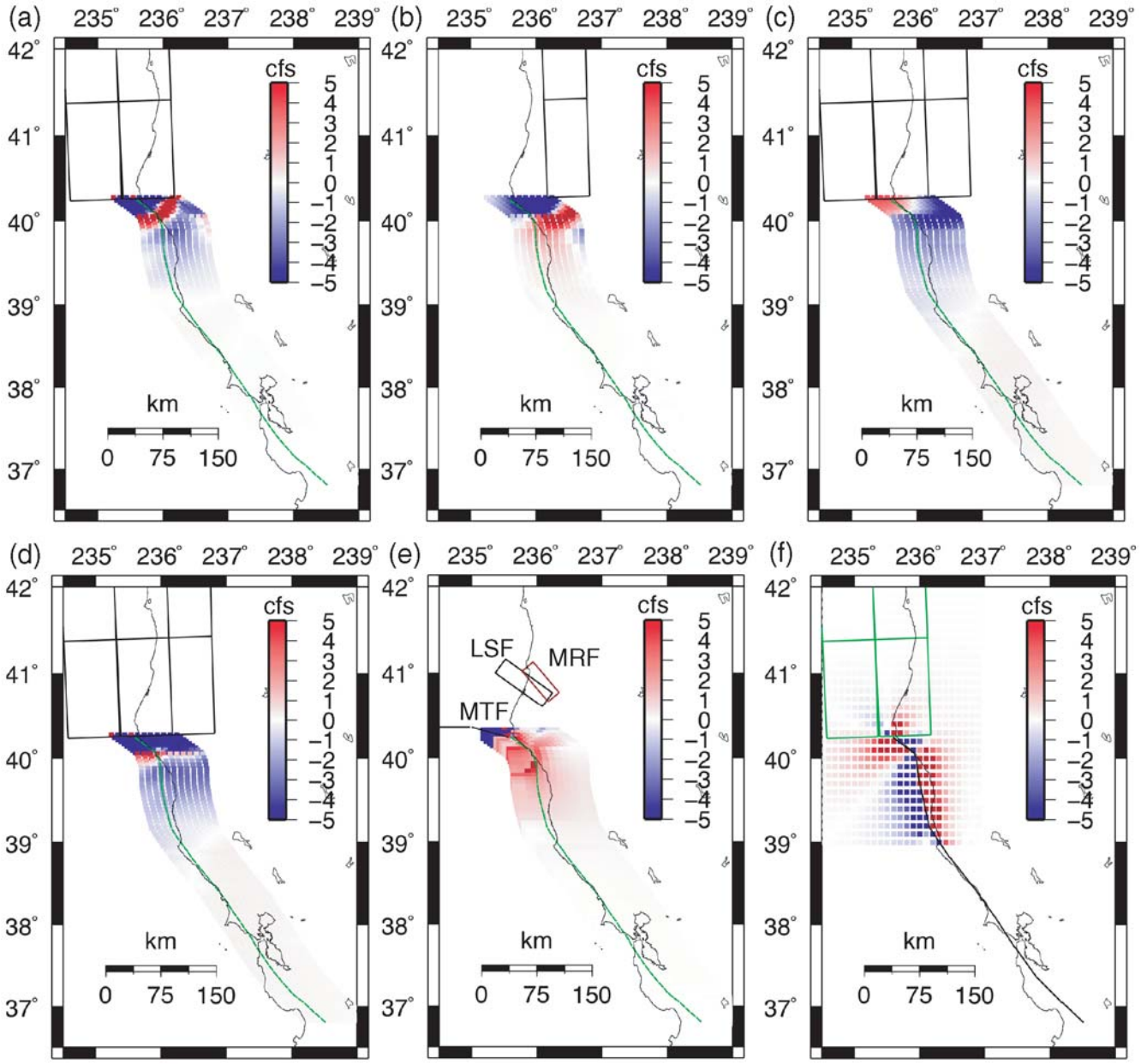

Figure 12. Comparison of CFS changes (bars) at 10-km depth on the NSAF from (a) coseismic deformation, (b) afterslip, (c) 60 yr of viscoelastic relaxation, (d) combined coseismic, afterslip, and viscoelastic relaxation, and (e) coseismic deformation and viscoelastic relaxation from MTF and LSF. Fault segments in black are source faults; green segments signify receiver faults. (f) CFS change on the Cascadia receiver faults from an NSAF earthquake.

Cascadia earthquakes follow NSAF events on average by 150 yr.

Could the temporal relationship between Cascadia and the NSAF be due to some of the turbidite events actually being the same source events, recorded on both sides of the triple junction? Indeed, it is possible that the thin mud turbidites could have been triggered in southern Oregon canyons by the NSAF and bear no relationship to Cascadia events. We consider this possibility less likely than Cascadia triggering, as the required triggering distances from the northern tip of the NSAF to Rogue (220 km), Klamath (180 km), and Trinidad (130 km) Canyon heads are 50%–240% greater than the 90-km distance from southern Cascadia to Noyo Canyon. Since Cascadia events did not trigger Noyo turbidity currents (see previous explanation and Goldfinger *et al.*, 2007), we consider NSAF triggering of Rogue, Smith, Klamath, or Trinidad Canyon turbidity currents unlikely. Triggering in the poorly known Eel Canyon may be possible, though the uppermost turbidite there has an age of ~233 yr (2σ 188–350), consistent with the A.D. 1700 Cascadia earthquake and suggesting no 1906 triggering occurred there. We note that the smaller undated events appear to be

more robust southward from Smith to Klamath to Trinidad canyons, which could support NSAF triggering. However, this equally well could be due to southward increases in submarine drainage areas or river discharge and sediment supply for these systems. In any case, only two of the thin mud turbidites that are not reported at both Cascadia land and marine sites are part of the post 3000-yr correlation shown in Figures 6 and 7. All other events are correlated too far north in Cascadia, and likely coincide with tsunami and subsidence deposits on land, precluding any connection to the NSAF. Similarly, the NSAF events are correlated southward for over 250 km both stratigraphically and more indirectly by their temporal relationship to land event ages from the Fort Ross, Vedanta, and Bolinas sites, making any direct triggering by Cascadia earthquakes unlikely.

Conclusions

We have tested the turbidite record along the Cascadia and NSAF continental margins for synchronous triggering of turbidity currents as a method for determining the origin of these deposits, whether from earthquake or other sources. We have used ^{14}C ages, relative dating tests at channel confluences, and direct correlation of physical properties to determine whether turbidites deposited in separate channel systems are correlative, that is, whether they were triggered by a common event. The NSAF late Holocene turbidite record examined thus far has passed these tests, and can be correlated with multiple proxies along multiple canyon systems from the MTJ to offshore San Francisco. Correlations of the youngest 10 events are improved by addition of color reflectance data to the geophysical proxies used for stratigraphic correlation.

Preliminary comparisons of our event ages with existing and in-progress work at onshore sites show good correspondence, further circumstantial evidence that the offshore record is primarily earthquake generated. During the last ~2100 yr, we observe 11 most likely correlative turbidites, including one likely generated by the 1906 earthquake, that can be traced between Noyo Canyon, near the MTJ, and Cordell Channel near Point Reyes. Using combined constraints from physical property correlation, radiocarbon ages, and interevent sedimentation, we conclude that it is likely that at least 8 of 11 NSAF events recorded both onshore and offshore in the past 2100 yr have rupture lengths of at least 250 km and extend from the MTJ region to near the latitude of San Francisco.

Onshore and offshore paleoseismic records from the Cascadia subduction zone suggest that margin-wide and segmented southern Cascadia earthquakes precede NSAF events by ~0–80 yr, averaging 25–45 yr for 13 of 15 probable earthquakes or 87% of NSAF events in the past 3000 yr, with two additional Cascadia events too poorly constrained for comparison. On the other hand, NSAF events precede Cascadia earthquakes on average by ~150–200 yr, most likely too long for a stress change effect.

Modeling of the static coseismic and both viscoelastic and afterslip-induced postseismic stress changes suggests that coseismic stress changes from Cascadia earthquakes are more than sufficient to trigger NSAF events, if they nucleate along the northernmost section of the NSAF near Point Delgada.

Acknowledgments

We thank the officers and crew of the Scripps vessels R/V Melville and R/V Revelle and the members of the 1999 and 2002 scientific parties. We thank David Schwartz, Mary Lou Zoback, Tom Fumal, Tina Niemi, Fred Pollitz, Alan Nelson, Rob Witter, Harvey Kelsey, and many others for insightful discussions on the NSAF and Cascadia faults; Alan Nelson, Tom Fumal, and Rob Witter for sharing unpublished data; and Harvey Kelsey and anonymous reviewers for thoughtful reviews that resulted in numerous improvements to the paper. We gratefully acknowledge funding by the U.S. National Science Foundation, Earth Sciences Division and by the U.S. Geological Survey National Earthquake Hazards Reduction Program. The authors acknowledge WesternGeco and the U.S. Geological Survey (USGS) for providing the seismic reflection data for the purpose of this research. Neither the data provider nor the USGS warrant the use of these data, nor make any claims or guarantees as to the accuracy of the data identification, acquisition parameters, processing methods, navigation, or database entries.

References

Abdelayem, A. L., K. Ikehara, and T. Yamazaki (2004). Flow path of the 1993 Hokkaido-Nansei-Oki earthquake seismoturbidite, southern margin of the Japan Sea north basin, inferred from anisotropy of magnetic susceptibility, *Geophys. J. Int.* **157,** 15–24.

Acharya, H. (1992). Comparison of seismicity parameters in different subduction zones and its implications for the Cascadia subduction zone, *J. Geophys. Res.* **97,** 8831–8842.

Adams, J. (1990). Paleoseismicity of the Cascadia subduction zone: evidence from turbidites off the Oregon-Washington margin, *Tectonics* **9,** 569–583.

Ando, M., and E. I. Balazs (1979). Geodetic evidence for aseismic subduction of the Juan de Fuca plate, *J. Geophys. Res.* **84,** 3023–3027.

Argus, D., and R. Gordon (2001). Present tectonic motion across the Coast Ranges and San Andreas fault system in central California, *Geol. Soc. Am. Bull.* **113,** 1580–1592.

Atwater, B. F. (1987). Evidence for great Holocene earthquakes along the outer coast of Washington State, *Science* **236,** 942–944.

Atwater, B. F., and E. Hemphill-Haley (1997). Recurrence intervals for great earthquakes of the past 3500 years at northeastern Willapa Bay, Washington, *U.S. Geol. Surv. Profess. Pap. 1576*, 108_pp.

Banerjee, P., F. Pollitz, and R. Bürgmann (2005). The size and duration of the Sumatra-Andaman earthquake from far-field static offsets, *Science* **308,** 1769–1772.

Brown, R. D. (1995). 1906 Surface Faulting on the San Andreas fault near Point Delgada, California, *Bull. Seismol. Soc. Am.* **85,** no. 1, 100–110.

Brudzinski, M. R., and R. A. Allen (2007). Segmentation in episodic tremor and slip all along Cascadia, *Geology* **35,** 907–910.

Carver, G. A. (2000). Paleoseismic geology of the southern part of the Cascadia subduction zone Penrose conference: great Cascadia earthquake tricentennial (program summary and abstracts), Oregon Department of Geology and Mineral Industries, Seaside, Oregon, 38–39.

Carver, G. A., and G. Plafker (1999). Cascadia subduction zone segmentation in the Mendocino triple junction region, *Seism. Res. Lett.* **70,** 245–246.

Castillo, D. A., and W. L. Ellsworth (1993). Seismotectonics of the San Andreas fault system between Point Arena and Cape Mendocino in northern California: implications for the development and evolution of a young transform, *J. Geophys. Res.* **98,** no. 4, 6543–6560.

Clarke, S. H., Jr., and G. A. Carver (1992). Late Holocene tectonics and paleoseismicity, southern Cascadia subduction zone, *Science* **255,** 188–191.

Curray, J. R., and R. D. Nason (1967). San Andreas fault north of Point Arena, California, *Geol. Soc. Am. Bull.* **78,** 413–418.

d'Alessio, M. A., I. A. Johansen, R. Bürgmann, D. A. Schmidt, and M. H. Murray (2005). Slicing up the San Francisco Bay Area: block kinematics and fault slip rates from GPS-derived surface velocities, *J. Geophys. Res.* **110,** B06403, doi 10.1029/2004JB003496.

Dallimore, A., R. E. Thomson, and M. A. Bertram (2005). Modern to late Holocene deposition in an anoxic fjord on the west coast of Canada: implications for regional oceanography, climate and paleoseismic history, *Mar. Geol.* **219,** no. 1, 47–60.

Dickinson, W. R., and W. S. Snyder (1979). The geometry of the triple junctions related to San Andreas transform, *J. Geophys. Res.* **84,** 561–572.

Dragert, H., R. D. Hyndman, G. C. Rogers, and K. Wang (1994). Current deformation and the width of the seismogenic zone of the northern Cascadia subduction thrust, *J. Geophys. Res.* **99,** 653–668.

Dziewonski, A. M., and D. L. Anderson (1981). Preliminary reference Earth model, *Phys. Earth Planet. Interiors* **25,** 297.

Field, M. E. (1984). The submarine landslide of 1980 off northern California, *U. S. Geol. Surv. Circ. 928*, 65–72.

Flueck, P., R. D. Hyndman, and K. Wang (1997). Three-dimensional dislocation model for great earthquakes of the Cascadia subduction zone, *J. Geophys. Res. B: Solid Earth Planets* **102,** 20,539–20,550.

Freed, A. M. (2005). Earthquake triggering by static, dynamic, and postseismic stress transfer, *Ann. Rev. Earth Planet. Sci.* **33,** 335–368.

Freymueller, J. T., M. H. Murray, P. Segall, and D. Castillo (1999). Kinematics of the Pacific–North American plate boundary zone, northern California, *J. Geophys. Res.* **104,** 7419–7441.

Fukuma, K. (1998). Origin and applications of whole-core magnetic susceptibility of sediments and volcanic rocks from Leg 152, *Proc. Ocean Drill. Prog.: Sci. Res.* **152,** 271–280.

Garcia-Orellana, J., E. Gràcia, A. Vizcaino, P. Masqué, C. Olid, F. Martínez Ruiz, E. Piñero, J. A. Sanchez-Cabeza, and J. J. Dañobeitia (2006). Identifying instrumental and historical earthquake records in the SW Iberian margin using ^{210}Pb turbidite chronology, *Geophys. Res. Lett.* **33,** L24601, doi 10.1029/2006GL028417.

Garfield, N., T. A. Rago, K. J. Schnebele, and C. A. Collins (1994). Evidence of a turbidity current in Monterey Submarine Canyon associated with the 1989 Loma Prieta earthquake, *Cont. Shelf Res.* **14,** no. 6, 673–686.

Goldfinger, C. (2007). DOGAMI Final Project Report 07-02, Paleoseismic slip history and geologic constraints on splay faulting and interplate coupling along the Cascadia subduction zone, Oregon State University, Corvallis, Oregon, 13 pp.

Goldfinger, C., L. D. Kulm, R. S. Yeats, C. Hummon, G. J. Huftile, A. R. Niem, C. G. Fox, and L. C. McNeill (1996). Oblique strike-slip faulting of the Cascadia submarine forearc: the Daisy Bank fault zone off central Oregon, in *Subduction Top to Bottom*, G. E. Bebout, D. Scholl, S. Kirby and J. P. Platt (Editors), American Geophysical Monograph 96, 65–74.

Goldfinger, C., L. D. Kulm, R. S. Yeats, L. C. McNeill, and C. Hummon (1997). Oblique strike-slip faulting of the central Cascadia submarine forearc, *J. Geophys. Res.* **102,** 8217–8243.

Goldfinger, C., M. E. Mackay, G. F. Moore, L. D. Kulm, R. S. Yeats, and B. Appelgate (1992). Transverse structural trends along the Oregon convergent margin: implications for Cascadia earthquake potential and crustal rotations, *Geology* **20,** 141–144.

Goldfinger, C., A. Morey, M. Erhardt, C. H. Nelson, J. Gutierrez-Pastor, R. Enkin, and A. Dallimore (2006). Cascadia great earthquake recurrence: rupture lengths, correlations and constrained OxCal analysis of event ages, in *Proc. U.S. Geol. Soc. Tsunami Sources Workshop*, 21–22 April 2006, M. Diggles, E. Geist and W. Lee (Editors), (available on CD-ROM).

Goldfinger, C., A. Morey, and C. H. Nelson (2006). Deep-water turbidites as Holocene earthquake proxies along the northern San Andreas fault system, *Seism. Res. Lett.* **77,** no. 2, 195–196.

Goldfinger, C., A. E. Morey, C. H. Nelson, J. Gutierrez-Pastor, J. E. Johnson, E. Karabanov, J. Chaytor, and A. Ericsson (2007). Rupture lengths and temporal history of significant earthquakes on the offshore and north coast segments of the northern San Andreas fault based on turbidite stratigraphy, *Earth Planet. Sci. Lett.* **254,** 9–27.

Goldfinger, C., C. H. Nelson, and J. Johnson (2003a). Holocene earthquake records from the Cascadia subduction zone and northern San Andreas fault based on precise dating of offshore turbidites, *Ann. Rev. Geophys.* **31,** 555–577.

Goldfinger, C., C. H. Nelson, and J. E. Johnson (2003b). Deep-water turbidites as Holocene earthquake proxies: the Cascadia subduction zone and northern San Andreas fault systems, *Ann. Geofis.* **46,** 1169–1194.

Goldfinger, C., C. H. Nelson, J. E. Johnson, and A. Morey (2003).Physical property correlations and radiocarbon ages illuminate Cascadia earthquake recurrence patterns (Abstract S42A-0144), *EOS Trans. AGU* **84,** no. 46 (Fall Meet. Suppl.), S42A-0144.

Goldfinger, C., C. H. Nelson, and J. E. Johnson (2004). Deep-water turbidites as Holocene earthquake proxies, *U.S. Geol. Soc. Northern San Andreas Fault System, San Andreas Fault Workshop*, Menlo Park, California.

Goldfinger, C., C. H. Nelson, J. E. Johnson, M. A. Arsenault, A. Eriksson, E. Karabanov, and J. Chaytor (2004). Physical property correlations from cascadia great earthquakes: what are they telling us about the triggering events? (Abstract OS21E-01), *EOS* **85,** no. 47 (Fall Meet. Suppl.), OS21E-01.

Goslar, T., W. O. van der Knaap, S. Hicks, M. Andric, J. Czernik, E. Goslar, S. Räsänen, and H. Hyötylä (2005). Radiocarbon dating of modern peat profiles: pre and postbomb 14c variations in the construction of agedepth models, *Radiocarbon* **47,** 115–134.

Grantz, A., R. L. Phillips, M. W. Mullen, S. W. Starratt, G. A. Jones, S. S. Naidu, and B. P. Finney (1996). Character, paleoenvironment, rate of accumulation, and evidence for seismic triggering of Holocene turbidites, Canada abyssal plain, Arctic Ocean, *Mar. Geol.* **133,** 51–73.

Griggs, G. B., and L. D. Kulm (1970). Sedimentation in Cascadia deep-sea channel, *Geol. Soc. Am. Bull.* **81,** 1361–1384.

Gutierrez-Pastor, J., H. C. Hans Nelson, C. Goldfinger, C. Escutia, and A. Morey (2007). Earthquake control and frequency of generation on the Cascadia and San Andreas active continental margins, SEPM Spec. Pap. on Turbidites, in press.

Hagstrum, J. T., B. F. Atwater, and B. L. Sherrod (2004). Paleomagnetic correlation of late Holocene earthquakes among estuaries in Washington and Oregon, *Geochem. Geophys. Geosys.* **5,** Q10001, doi 10.1029/2004GC000736.

Hallett, D. J., L. V. Hills, and J. J. Clague (1997). New accelerator mass spectrometry radiocarbon ages for the Mazama tephra layer from Kootenay National Park, British Columbia, Canada, *Can. J. Earth Sci.* **34,** 1202–1209.

Heaton, T. H., and H. Kanamori (1984). Seismic potential associated with subduction in the northwestern United states, *Bull. Seismol. Soc. Am.* **74,** 993–941.

Heezen, B. C., and M. Ewing (1952). Turbidity currents and submarine slumps, and the 1929 Grand Banks earthquake, *Am. J. Sci.* **250,** 849–873.

Hu, Y., K. Wang, J. He, J. Klotz, and G. Khazaradze (2004). Three-dimensional viscoelastic finite element model for postseismic deformation of the great 1960 Chile earthquake, *J. Geophys. Res.* **109,** B12403, doi 10.1029/2004JB003163.

Hughen, K., S. Lehman, J. Southon, J. Overpeck, O. Marchal, C. Herring, and J. Turnbull (2004). 14C activity and global carbon cycle changes over the past 50,000 years, *Science* **303,** 202–207.

Inouchi, Y., Y. Kinugasa, F. Kumon, S. Nakano, S. Yasumatsu, and T. Shiki (1996). Turbidites as records of intense palaeoearthquakes in Lake Biwa, Japan, *Sed. Geol.* **104,** 117–125.

Iwaki, H., A. Hayashida, N. Kitada, H. Ito, S. Suwa, and K. Takemura (2004). Stratigraphic correlation of samples from the Osaka Bay off Kobe based on magnetic properties and its implication for tectonic activity of the Osaka-Wan fault for the last 6300 years (Abstract GP41C-0053), *EOS* **84,** (Fall Meet. Suppl.) GP41C-0053.

Jennings, C. W. (1995). New fault map of California and adjacent areas, *Calif. Geol.* **48,** no. 2, 31–42.

Johnson, J. (2004). Deformation, fluid venting, and slope failure at an active margin gas hydrate province, Hydrate Ridge, Cascadia accretionary wedge, *Ph.D. Thesis*, Oregon State University, Corvallis, 145 pp.

Karlin, R. E., M. Holmes, S. E. B. Abella, and R. Sylwester (2004). Holocene landslides and a 3500-year record of Pacific Northwest earthquakes from sediments in Lake Washington, *Geol. Soc. Am. Bull.* **116,** no. 1–2, 94–108.

Kastens, K. A. (1984). Earthquakes as a triggering mechanism for debris flows and turbidites on the Calabrian Ridge, *Mar. Geol.* **55,** 13–33.

Kelsey, H. M., A. R. Nelson, E. Hemphill-Haley, and R. C. Witter (2005). Tsunami history of an Oregon coastal lake reveals a 4600 yr record of great earthquakes on the Cascadia subduction zone, *Geol. Soc. Am. Bull.* **117,** 1009–1032.

Kelsey, H. M., R. C. Witter, and E. Hemphill-Haley (2002). Plate-boundary earthquakes and tsunamis of the past 5500 yr, Sixes River estuary, southern Oregon, *Geol. Soc. Am. Bull.* **114,** 298–314.

Kelson, K., A. Strieg, R. Koehler, and K. Kang (2006). Timing of late Holocene paleoearthquakes on the northern San Andreas fault at the Fort Ross Orchard site, Sonoma County, California, *Bull. Seismol. Soc. Am.* **96,** no. 3, 1012–1028.

Knudsen, K. L., R. C. Witter, C. E. Garrison-Laney, J. N. Baldwin, G. A. Carver, L. B. Grant, and W. R. Lettis (2002). Past earthquake-induced rapid subsidence along the northern San Andreas fault: a paleoseismological method for investigating strike-slip faults, *Bull. Seismol. Soc. Am.* **92,** 2612–2636.

Kovanen, D. J., and D. J. Easterbrook (2002). Paleodeviations of radiocarbon marine reservoir values for the northeast Pacific, *Geology* **30,** 243–246.

Lawson, A. C. (1908). *The California Earthquake of April 18, 1906: Report of the State Earthquake Investigation Commission*, Publ. 87, Vol. **1–2,** Carnegie Institution of Washington, Washington, D.C, (reprinted 1969).

Lees, J. A., R. J. Fowler, and P. G. Appleby (1998). Mineral magnetic and physical properties of surficial sediments and onshore samples from the southern basin of Lake Baikal, Siberia, *J. Paleolimnol.* **20,** no. 2, 175–186.

Leonard, L. J., R. D. Hyndman, and S. Mazzotti (2004). Coseismic subsidence in the 1700 great Cascadia earthquake: coastal estimates versus elastic dislocation models, *Geol. Soc. Am. Bull.* **116,** 655–670.

Lovlie, R., and P. van Veen (1995). Spec. Pub. 98, Magnetic susceptibility of a 180 m sediment core: reliability of incremental sampling and evidence for a relationship between susceptibility and gamma activity, in *Palaeomagnetic Applications in Hydrocarbon Exploration and Production*, P. Turner and A. Turner (Editors), Geological Society, London, 259–266.

Lyle, M., A. C. Mix, and N. G. Pisias (2002). Patterns of CaCO3 deposition in the eastern tropical Pacific Ocean for the last 150 kyr: evidence for a southeast Pacific depositional spike during marine isotope stage (MIS) 2, *Paleoceanography* **17,** no. 2, 1013, doi 10.1029/2000PA000538.

McCaffrey, R. (1997). Influences of recurrence times and fault zone temperatures on the age-rate dependence of subduction zone seismicity, *J. Geophys. Res.* **102,** 22,839–22,854.

McCaffrey, R., M. D. Long, C. Goldfinger, P. C. Zwick, J. L. Nabelek, C. K. Johnson, and C. Smith (2000). Rotation and plate locking at the southern Cascadia subduction zone, *Geophys. Res. Lett.* **27,** 3117–3120.

McCaffrey, R., A. Qamar, R. W. King, R. W. Wells, G. Khazaradze, C. Williams, C. Stevens, J. J. Vollick, and P. C. Zwick (2007). Fault locking, block rotation and crustal deformation in the Pacific Northwest, *Geophys. J. Int.* **169,** 1315–1340.

McCrory, P. A. (1996). Evaluations of fault hazards, northern coastal California, *U.S. Geol. Surv. Open-File Rept. 96-656*, 87 pp.

McCubbin, D. G. (1982). Barrier-Island and Strand-Plain Facies, in *Sandstone Depositional Environment*, P. A. Scholle and D. Spearing (Editors), AAPG, Tulsa, Oklahoma, 247–279.

McLaughlin, R. J., K. R. LaJoie, D. H. Sorg, S. D. Morrison, and J. A. Wolfe (1983). Tectonic uplift of a middle Wisconsin marine platform near the Mendocino triple junction, California, *Geology* **11,** 35–39.

Morey, A., C. Goldfinger, C. H. Nelson, J. Chaytor, J. E. Johnson, and A. Ericsson (2003). Turbidite based earthquake record along the northern San Andreas fault (Abstract T41C-02), *EOS* **84,** no. 46 (Fall Meet. Suppl.), T51C-02.

Nakajima, T., and Y. Kanai (2000). Sedimentary features of seismoturbidites triggered by the 1983 and older historical earthquakes in the eastern margin of the Japan Sea, *Sediment. Geol.* **135,** 1–19.

Nalbant, S. S., S. Steacy, K. Sieh, D. Natawidjaja, and J. McCloskey (2005). Earthquake risk on the Sunda trench, *Nature* **435,** 756–757.

Nederbragt, A. J., R. B. Dunbar, A. T. Osborn, A. Palmer, J. W. Thurow, and T. Wagner (2006). Spec. Pub. 267, Sediment colour analysis from digital images and correlation with sediment composition, in *New Techniques in Sediment Core Analysis*, R. G. Rothwell and F. R. Rack (Editors), Geological Society, London, 112–128.

Nelson, C. H. (1976). Late Pleistocene and Holocene depositional trends, processes and history of Astoria Deep-sea Fan, *Mar. Geol.* **20,** 129–173.

Nelson, C. H., P. R. Carlson, and C. R. Bacon (1988). The Mount Mazama climactic eruption (~6900 yr BP) and resulting convulsive sedimentation on the Crater Lake caldera floor, continent, and ocean basin, Geol. Soc. Am. Spec. Pap. 229, 37–57.

Nelson, C. H., C. Goldfinger, J. E. Johnson, and G. Dunhill (2000). Variation of modern turbidite systems along the subduction zone margin of Cascadia Basin and implications for turbidite reservoir beds, in *Deep-Water Reservoirs of the World: 20th Annual Res. Conf, Gulf Coast Section Society of Economic Paleontologists and Mineralogists*, P. W. Weimer and C. H. Nelson (Editors), 31 pp.

Nelson, A. R., H. M. Kelsey, and R. C. Witter (2006). Great earthquakes of variable magnitude at the Cascadia subduction zone, *Quat. Res.* **65,** 354–365.

Nelson, C. H., L. D. Kulm, P. R. Carlson, and J. R. Duncan (1968). Mazama ash in the northeastern Pacific, *Science* **161,** 47–49.

Niemi, T. M., and Z. Ben-Avraham (1994). Evidence for Jericho earthquakes from slumped sediments of the Jordan River delta in the Dead Sea, *Geology* **22,** 395–398.

Niemi, T. M., and N. T. Hall (1992). Late Holocene slip rate and recurrence of great earthquakes on the San Andreas fault in northern California, *Geology* **20,** 195–198.

Oleskevich, D. A., R. D. Hyndman, and K. Wang (1999). The updip and downdip limits to great subduction earthquakes: thermal and structural models of Cascadia, south Alaska, SW Japan, and Chile, *J. Geophys. Res. B: Solid Earth Planets* **104,** 14,965–14,991.

Oppenheimer, D., G. Beroza, G. Carver, L. Dengler, J. Eaton, L. Gee, F. Gonzalez, A. Jayko, W. H. Li, M. Lisowski, M. Magee, G. Marshall, M. Murray, R. McPhereson, B. Romanowicz, K. Satake, R. Simpson, P. Somerville, R. Stein, and D. Valentine (1993). The Cape Mendocino, California, earthquakes of April 1992: subduction at the triple junction, *Science* **261,** 433–438.

Petersen, M. D., W. A. Bryant, C. H. Cramer, T. Cao, M. S. Reichle, A. D. Frankel, J. J. Lienkaemper, P. A. McCrory, and D. P. Schwartz (1996). Probabilistic seismic hazard assessment for the State of California, *Calif. Div. Mines Geol. Open-File Rept. 96-08* (published jointly as *U.S. Geol. Surv. Open-File Rept. 96-706*).

Pollitz, F. F. (1992). Postseismic relaxation theory on the spherical earth, *Bull. Seismol. Soc. Am.* **82,** 422–453.

Pollitz, F. F. (1996). Coseismic deformation from earthquake faulting on a layered spherical earth, *Geophys. J. Int.* **125,** 1–14.

Pollitz, F., R. Bürgmann, and P. Banerjee (2006). Post-seismic relaxation following the great 2004 Sumatra-Andaman earthquake on a compressible self-gravitating Earth, *Geophys. J. Int.* **167,** 397–420, doi 10.1111/j.1365-246X.2006.03018.x.

Pollitz, F., R. Bürgmann, and B. Romanowicz (1998). Viscosity of oceanic asthenosphere inferred from remote triggering of earthquakes, *Science* **280,** 1245–1249.

Pollitz, F. F., P. A. McCrory, J. L. Svarc, and J. Murray (2008). Dislocation models of interseismic deformation in the western United States, *J. Geophys. Res.*, doi 10.1029/2007JB005174, in press.

Polonia, A., L. Gasperini, A. Amorosi, E. Bonatti, G. Bortoluzzi, N. Cagatay, L. Capotondi, M. H. Cormier, N. Gorur, C. McHugh, and L. Seeber (2004). Holocene slip rate of the North Anatolian fault beneath the Sea of Marmara, *Earth Planet. Sci. Lett.* **227,** 411–426.

Prentice, C. S. (1989). Earthquake geology of the northern San Andreas fault near Point Arena, California, *Ph.D. Thesis*, California Institute of Technology, Pasadena, California, 252 pp.

Prentice, C., R. Langridge, and D. Merritts (2000). Paleoseismic and quaternary tectonic studies of the San Andreas fault from Shelter Cove to Fort Ross in *3rd Conference on Tectonic Problems of the San Andreas Fault System*, R. L. Kovach and G. Bokelmann (Editors), Stanford University, Stanford, California.

Prentice, C. S., D. J. Merritts, and E. C. Beutner (1999). Northern San Andreas fault near Shelter Cove, California, *Geol. Soc. Am. Bull* **111,** no. 4, 512–523.

Ramsey, C. B. (1995). Radiocarbon calibration and analysis of stratigraphy: the OxCal program, *Radiocarbon* **37,** no. 2, 425–430.

Ramsey, C. B. (2001). Development of the radiocarbon program OxCal, *Radiocarbon* **43,** 355–363.

Reimer, P. J., M. G. L. Baillie, E. Bard, A. Bayliss, J. W. Beck, C. J. H. Bertrand, P. G. Blackwell, C. E. Buck, G. S. Burr, K. B. Cutler, P. E. Damon, R. L. Edwards, R. G. Fairbanks, M. Friedrich, T. P. Guilderson, A. G. Hogg, K. A. Hughen, B. Kromer, F. G. McCormac, S. W. Manning, C. B. Ramsey, R. W. Reimer, S. Remmele, J. R. Southon, M. Stuiver, S. Talamo, F. W. Taylor, J. van der Plicht, and C. E. Weyhenmeyer (2004). IntCal04 Terrestrial radiocarbon age calibration, 26–0 ka BP, *Radiocarbon* **46,** 1029–1058.

Rivera, J., E. B. Karabanov, D. F. Williams, V. Buchinskyi, and M. Kuzmin (2006). Lena River discharge events in sediments of Laptev Sea, Russian Arctic, *Estuar. Coast. Shelf Sci.* **66,** 185–196.

Rogerson, M., P. P. E. Weaver, E. J. Rohling, L. J. Lourens, J. W. Murray, and A. Hayes (2006). Colour logging as a tool in high-resolution palaeoceanography, in *New Techniques in Sediment Core Analysis*, R. G. Rothwell and F. R. Rack (Editors), Volume Geol. Soc. Spec. Pub. 267, Geological Society of London, London, U.K., 99–112.

Rydelek, P. A., and I. S. Sacks (1999). Large earthquake occurrence affected by small stress changes, *Bull. Seismol. Soc. Am.* **89,** 822–828.

Satake, K., K. Shimazaki, Y. Tsuji, and K. Ueda (1996). Time and size of a giant earthquake in Cascadia inferred from Japanese tsunami records of January, 1700, *Nature* **379,** 246–249.

Satake, K., K. Wang, and B. F. Atwater (2003). Fault slip and seismic moment of the 1700 Cascadia earthquake inferred from Japanese tsunami descriptions, *J. Geophys. Res. B: Solid Earth Planets* **108,** 2325, doi 10.1019/2003JB002521.

Sauber, J. W., W. Thatcher, S. C. Solomon, and M. Lisowski (1994). Geodetic slip-rate for the eastern California shear zone and the recurrence time for Mojave Desert earthquakes, *Nature* **367,** 264–266.

Schnellmann, M., F. S. Anselmetti, D. Giardini, and S. N. Ward (2002). Prehistoric earthquake history revealed by lacustrine slump deposits, *Geology* **30,** no. 12, 1131–1134.

Segall, P. (2002). Integrating geologic and geodetic estimates of slip rate on the San Andreas fault system, *Int. Geol. Rev.* **44,** no. 1, 62–82.

Segall, P., and D. Castillo (1999). Kinematics of the Pacific-North American plate boundary zone, northern California, *J. Geophys. Res.* **104,** 7419–7441.

Shiki, T., F. Kumon, Y. Inouchi, Y. Kontani, T. Sakamoto, M. Tateishi, H. Matsubara, and K. Fukuyama (2000). Sedimentary features of the seismo-turbidites, Lake Biwa, Japan, *Sed. Geol.* **135,** 37–50.

Smith, C. R., R. H. Pope, D. J. DeMaster, and L. Magaard (1993). Age-dependent mixing of deep-sea sediments, *Geochim. Cosmochim. Acta* **57,** 1473–1488.

Song, S., G. C. Beroza, and P. Segall (2008). A unified source model for the 1906 San Francisco earthquake, *Bull. Seismol. Soc. Am.* **98,** no. 2, 823–831.

Stein, R. S., and M. Lisowski (1983). The 1979 Homestead Valley earthquake sequence, California: control of aftershock and postseismic deformation, *J. Geophys. Res.* **88,** 6477–6490.

Stein, R. S., G. C. P. King, and J. Lin (1992). Change in failure stress on the southern San Andreas fault system caused by the 1992 M 7.4 Landers earthquake, *Science* **258,** 1325–1328.

St-Onge, G., T. Mulder, D. J. W. Piper, C. Hillaire-Marcel, and J. S. Stoner (2004). Earthquake and flood-induced turbidites in the Saguenay Fjord (Québec): a Holocene paleoseismicity record, *Quat. Sci. Rev.* **23,** 283–294.

Stuiver, M., and T. F. Braziunas (1993). Modeling atmospheric 14C influences and 14C ages of marine samples to 10,000 BC, *Radiocarbon* **35,** 137–189.

Thatcher, W., G. Marshall, and M. Lisowski (1997). Resolution of fault slip along the 470 km long rupture of the great 1906 San Francisco earthquake, *J. Geophys. Res.* **102,** 5353–5367.

Thomson, J., G. T. Cook, R. Anderson, A. B. Mackenzie, D. D. Harkness, and I. N. McCave (1995). Radiocarbon age offsets in different-sized carbonate components of deep-sea sediments, *Radiocarbon* **37,** no. 2, 91–103.

Toda, S., R. S. Stein, P. A. Reasenberg, J. H. Dieterich, and A. Yoshida (1998). Stress transferred by the 1995 $M_w = 6.9$ Kobe, Japan, shock: effect on aftershocks and future earthquake probabilities, *J. Geophys. Res. B: Solid Earth Planets* **103,** 24,543–24,565.

Ward, S. N., and S. D. B. Goes (1993). How regularly do earthquakes recur? A synthetic seismicity model for the San Andreas fault, *Geophys. Res. Lett.* **20,** no. 19, 2131–2134.

Weldon, R. J., K. M. Scharer, T. E. Fumal, and G. P. Biasi (2004). Wrightwood and the earthquake cycle: what a long recurrence record tells us about how faults work, *Geol. Soc. Am. Today* **14,** no. 9, 4–10.

Wheatcroft, R. A. (1992). Experimental tests for particle size-dependent bioturbation in the deep ocean, *Limnol. Oceanogr.* **37,** 90–104.

Working Group on California Earthquake Probabilities (2003). Earthquake probabilities in the San Francisco Bay region: 2003 to 2032, *U.S. Geol. Surv. Open-File Rept. 03-214*, 235 pp.

Wynn, R. B., and D. G. Masson (2003). Canary Islands landslides and tsunami generation, in *Proc. 1st Int. Symposium on Submarine Mass Movements and their Consequences, Nice*, J. Locat and J. Meinert (Editors), Kluwer, Dordrecht, 325–332.

Wynn, R. B., P. P. E. Weaver, D. G. Masson, and D. A. V. Stow (2002). Turbidite depositional architecture across three interconnected deep-water basins on the north-west African margin, *Sedimentology* **49,** no. 4, 669–695.

Zdanowicz, C. M., G. A. Zielinski, and M. S. Germani (1999). Mount Mazama eruption: calendrical age verified and atmospheric impact assessed, *Geology* **27,** 621–624.

Zhang, H., T. Niemi, and T. Fumal (2006). A 3000-year record of earthquakes on the northern San Andreas fault at the Vedanta Marsh site, Olema, *Calif. Seism. Res. Lett.* **77,** no. 2, 248.

Zoback, M. L., R. C. Jachens, and J. A. Olson (1999). Abrupt along-strike change in tectonic style: San Andreas fault zone, San Francisco peninsula, *J. Geophys. Res.* **104,** 10719–10742.

Zweck, C., J. T. Freymueller, and S. C. Cohen (2002). The 1964 great Alaska earthquake: present day and cumulative postseismic deformation in the western Kenai Peninsula, *Phys. Earth. Planet. Interiors* **132,** 5–20.

Oregon State University
College of Oceanic and Atmospheric Sciences
104 Ocean Admin. Bldg.
Corvallis, Oregon 97331
gold@coas.oregonstatet.edu
drewerikssson@yahoo.com
jchaytor@whoi.edu
(C.G., A.E.M., A.E., J.D.C., J.P.)

Department of Earth and Planetary Science
307 McCone Hall
Univ. of California, Berkeley
Berkeley, California 94720-4767
burgmann@seismo.berkeley.edu
(K.G., R.B.)

University of New Hampshire
Department of Earth Sciences
56 College Rd.
Durham, New Hampshire 03824-3589
joel.johnson@unh.edu
(J.E.J.)

Instituto Andaluz de Ciencias de la Tierra (IACT), CSIC-Univ. de Granada
Campus de Fuentenueva
s/n 18002 Granada, Spain
odp@ugr.es
(C.H.N., J.G.)

Institute of Geochemistry
Siberian Branch of Russian Academy of Sciences
1A Favorsky St.
Irkutsk 664003, 22 Russia 29208
lenadelta2002@yahoo.com
(E.K.)

Centre Mediterrani d'Investigacions Marines i Ambientals Unitat de Tecnologia Marina (CSIC)
Passeig Marítim de la Barceloneta, 37-49
08003 Barcelona, Spain
egracia@cmima.csic.es
(E.G.)

Manuscript received 12 March 2007